OPEN ACCESS
IOP Publishing | International Atomic Energy Agency
Nuclear Fusion
Nucl. Fusion **66** (2026) 026013 (18pp)
https://doi.org/10.1088/1741-4326/ae27e3

Global gyrokinetic particle simulation of kinetic ballooning modes with energetic ions

W.J. Sun[1], J. Bao[1,*], C. Dong[1], W.L. Zhang[1,*], G. Dong[2], Z. Lin[3], J.T. Cao[1], Z.Y. Qiu[4], H.S. Cai[5] and D. Li[1]

[1] Institute of Physics, Chinese Academy of Sciences, Beijing 100190, China
[2] Energy Singularity Co., Ltd, Shanghai, China
[3] University of California, Irvine, CA 92697, United States of America
[4] Institute of Plasma Physics, Chinese Academy of Sciences, Hefei 230031, China
[5] University of Science and Technology of China, Hefei 230026, China

E-mail: jbao@iphy.ac.cn and wzhang@iphy.ac.cn

Received 3 September 2025, revised 12 November 2025
Accepted for publication 4 December 2025
Published 30 December 2025

Abstract

Interactions between energetic ions (EIs) and kinetic ballooning modes (KBMs) are inevitable in fusion reactors characterized by high-β plasmas with a large population of alpha particles ($\beta_h \sim \beta_{e,i}$, where $\beta_{h,e,i} = 2\mu_0 p_{h,e,i}/B_0^2$). In this work, the effects of EIs on KBM stability are investigated using first-principles gyrokinetic simulations, which demonstrate the roles of magnetohydrodynamic (MHD) ballooning-interchange drive, wave–particle resonance and orbital effects in several parameter regimes of practical interest. In particular, it is found that EI–KBM interactions are mostly determined by three dimensionless parameters: the EI–thermal electron temperature ratio T_h/T_e, the KBM perpendicular wave vector normalized by EI orbit width $k_\theta \rho_d$ and the EI pressure ratio β_h, which are associated with resonance condition, finite orbit width (FOW) screening and EI drive strength for Alfvénic modes. For typical orderings of $T_h/T_e \gg 1$ and $\beta_h \sim \beta_{e,i}$, $k_\theta \rho_d$ becomes crucial for relevant physical processes. (i) In the short-wavelength regime of $k_\theta \rho_d \gg 1$, the response of EIs to KBM electromagnetic fluctuations is greatly reduced due to strong FOW screening, which leads to a weakly stabilizing effect on KBMs via thermal ion dilution, despite the large β_h. (ii) In the long-wavelength regime of $k_\theta \rho_d \ll 1$, passing EIs can non-perturbatively destabilize KBMs through transit motion resonance, attributed to the fact that large poloidal and toroidal frequencies mostly cancel each other and satisfy $\omega = n\omega_\phi - p\omega_\theta$ locally around $q = p/n$ rational surfaces (p is an integer), while the net response of trapped EIs is near zero due to the mismatch of resonance conditions. For minor ion species characterized by $T_h/T_e \gtrsim 1$, such as helium ash, FOW screening is modest with $k_\theta \rho_d \sim 1$ and the drive strength is perturbative with $\beta_h \ll \beta_{e,i}$, which drive KBMs through MHD ballooning-interchange and wave–particle resonance similar to thermal ions. These findings are helpful for understanding the effects of alpha particles and helium ash on KBM stability and plasma confinement in future fusion reactors.

* Authors to whom any correspondence should be addressed.

Keywords: kinetic ballooning mode, energetic ion, phase space, wave particle resonance

(Some figures may appear in colour only in the online journal)

1. Introduction

The kinetic ballooning mode (KBM) is a typical drift Alfvén wave (DAW) instability driven by both magnetohydrodynamic (MHD) ballooning-interchange in reactive-type and kinetic wave–particle resonance in dissipative-type [1–3], and plays an important role in the formation of an internal transport barrier (ITB) [4] and edge pedestal [5]; it is an active research topic [6]. Specifically, the KBM can be destabilized by increasing the pressure gradient above a critical value, which induces particle and energy transport in the ion channel instead of the electrostatic ion temperature gradient (ITG) mode, since the latter suffers significant finite-β stabilization ($\beta = 2\mu_0 p/B_0^2$) [7]. Therefore the KBM is considered as a dominant factor preventing increase in the plasma pressure in fusion devices. In burning plasmas, there are large numbers of energetic ions (EIs) generated by auxiliary heating and the fusion reaction, which can drive and/or interact with DAW instabilities over a wide range of toroidal mode numbers (n) and frequencies (ω), resulting in changes in the stability boundary in parameter space. In turn, these instabilities can induce EI losses through wave–particle resonance and degrade overall plasma confinement. In order to achieve high-performance fusion plasmas, an in-depth understanding of the impacts of EIs on the stability of the KBM is required; the physical mechanism of this could be complicated due to the strong coupling of EIs with thermal plasmas in the regime $\beta_h \sim \beta_{e,i}$.

Theoretical efforts were made in earlier studies to explain various effects of EIs on KBM stability. The individual EI diamagnetic drift and finite Larmor radius (FLR) have been shown to induce stabilization effects on ballooning modes in the fluid limit [8, 9]. Based on the kinetic energy principle, Rosenbluth *et al* clarified that trapped EIs can destabilize the KBM through the fluid term of δW_f, while stabilizing it through the kinetic term of δW_k in the limit of $\omega \ll n\omega_{\rm pre}$ ($\omega_{\rm pre}$ is the EI precession frequency) [10]. Biglari and Chen studied the effects of wave–particle resonance for both circulating and trapped EIs, which are found to destabilize the KBM when the characteristic frequencies are close to the mode frequency [11]. Tsai and Chen analyzed resonant excitations of KBMs by EIs with further including the effect of the finite orbit width (FOW), and found the existence of the MHD gap mode and energetic-particle continuum mode [12]. Spong *et al* carried out numerical studies by solving the EI–KBM integro-differential eigenmode equations based on the gyrokinetic model, and found that the ballooning mode stability boundaries could be degraded by trapped EIs through destabilization of the precessional drift resonance [13, 14]. In recent years, significant progress on EI mitigation of electrostatic micro-turbulence and anomalous transport has been achieved. It is worth mentioning that recent experimental results show that ITG turbulence can be stabilized by a large EI fraction, which effectively reduces anomalous transport and enables the plasma temperature to exceed 100 million kelvin up to 20 s [15]. Various physics mechanisms of EI stabilization of ITG turbulence are revealed by gyrokinetic simulations thanks to the development of supercomputing techniques, such as thermal ion dilution, finite-β stabilization, wave–particle resonance etc [7, 16]. However, given the physical complexity, the impacts of EI on KBM stability and corresponding turbulent transport have been much less investigated by global gyrokinetic simulations, although the KBM is considered to be an important candidate for restricting the transport barriers and limiting fusion performance.

In order to delineate the underlying physical mechanisms of EI–KBM interaction in candidate regimes of operation, we perform numerical studies using a first-principles gyrokinetic toroidal code GTC [17], which has been successfully applied in linear [18] and nonlinear [19] KBM physics. In particular, a new gyrokinetic EI model is formulated and implemented in GTC based on the Chen–Hasegawa theory [20], which splits the perturbed distribution into an adiabatic fluid convection response δf_h^A and a non-adiabatic kinetic response δK_h as $\delta f_h = \delta f_h^A + \delta K_h$; these are responsible for MHD ballooning-interchange drive in reactive-type and wave-particle resonance drive in dissipative-type, respectively. The KBM dispersion relation and mode structure and EI $|\delta f|^2$ intensity and perturbed pressure are obtained with different T_h/T_e and m_h/m_p values, covering a wide domain of EI pressure ratios β_h, dimensionless orbit widths $k_\theta \rho_d$ and various wave–particle resonances. Our findings demonstrate that for typical EI parameters of $T_h/T_e \gg 1$ and $\beta_h \sim \beta_{e,i}$ in present-day tokamaks and future fusion reactors, the EI response to KBM electromagnetic fluctuations is near zero in the short-wavelength regime of $k_\theta \rho_d \gg 1$ due to strong FOW screening and lack of resonance conditions; this perturbatively affects KBM stability via thermal ion dilution, despite the large β_h. The influence of EIs on the KBM becomes non-perturbative in the long-wavelength regime of $k_\theta \rho_d \ll 1$, which is characterized by a peculiar passing EI resonance process in the high-energy regime, resulting in the strong destabilization of the KBM with the mode structure adapting to the radial profile of the EI equilibrium pressure gradient. In addition, when the EI temperature is close to that of the bulk plasma with $T_h/T_e \gtrsim 1$, such as helium ash, EI fluid and kinetic responses accumulate in the low-energy regime and destabilize the KBM, with the growth rate increment being proportional to β_h, similar to thermal ion dynamics for KBM excitation [21, 22]. The nonlinear transport properties of EIs due to KBMs in the above regimes are also presented. It should be pointed out that we remove magnetic compressibility $\delta B_\parallel$ in this work, which is

shown to induce modest destabilization effects on the KBM through cancellation of drift reversal [18, 23, 24].

The remainder of this paper is organized as follows. Two gyrokinetic EI models are introduced in section 2 using the conventional δf-method and split scheme based on the Chen–Hasegawa theoretical framework. In section 3, linear and nonlinear KBM simulation results with scanning EI parameters are presented, including the KBM dispersion relation, mode structure and nonlinear saturation amplitude, and corresponding EI $|\delta f|^2$-intensity, perturbed pressure and nonlinear transport diffusivity due to KBM turbulence. A summary is given in section 4. In the appendix, the trapped EI fluid and kinetic responses are analytically derived, consistent with GTC simulation of their mutual cancellation in the low-frequency $\omega \ll n\omega_{\rm pre}$ and long-wavelength $k_\theta \rho_d \ll 1$ limits.

2. Physical model

In section 2.1 we describe the GTC physics model used in simulations; the thermal ions and EIs are described by gyrokinetic equations with the conventional δf-method and the thermal electrons are described by a massless fluid model in the lowest order for ion-scale drift-Alfvénic instability, which is able to preserve the essential factors of MHD ballooning-interchange and the ion kinetic effects such as FLR, FOW and various wave–particle resonances. Note that the EI model using the conventional δf-method is referred to as EI model A. In section 2.2, the gyrokinetic model is reformulated for EIs by splitting the perturbed distribution into adiabatic and non-adiabatic parts corresponding to MHD ballooning-interchange and kinetic particle compression (KPC) respectively, which enables the analysis of their independent roles. The EI model using a split scheme is referred to as EI model B, which is consistent with the Chen–Hasegawa theory and can be efficient for analyzing the underlying mechanisms of the impact of EIs on KBM instability.

2.1. Gyrokinetic ion and fluid electron electromagnetic model (EI model A: conventional δf-method)

In GTC electromagnetic simulations, the gyrokinetic model is widely applied for ion species, and the electron species dynamics can be described by a fluid–kinetic hybrid model that solves the drift kinetic equation based on the expansion method using the small parameter $\delta \sim \omega/\left(k_{||}v_{||}\right) < 1$ [25, 26], which gives the fluid solution in the lowest order and kinetic corrections in the higher order. As an alternative method, the conservative scheme is developed to solve the drift kinetic equation for electrons directly without approximation; it treats fluid and kinetic parts on an equal footing [27]. It should be pointed out that both the fluid–kinetic hybrid scheme and the conservative scheme can reduce to the same massless fluid model for electrons, which retains the effects of a finite parallel electric field $\delta E_{||}$ and fluid convection associated with density/temperature gradients and is appropriate for KBM simulations. For the reader's convenience and completeness of the paper, we first present the GTC gyrokinetic ion and massless fluid electron electromagnetic model equations used in this work.

The gyrokinetic Vlasov equation for ion species uses gyrocenter position $\mathbf{R}$, parallel velocity $v_{||}$ and magnetic moment μ as the independent coordinates in five-dimensional phase space $\left(\mathbf{R}, v_{||}, \mu\right)$ as

$$\left[\frac{\partial}{\partial t} + \dot{\mathbf{R}}\cdot\nabla + \dot{v}_{||}\frac{\partial}{\partial v_{||}}\right] f_\alpha\left(\mathbf{R}, v_{||}, \mu, t\right) = 0, \tag{1}$$

$$\dot{\mathbf{R}} = v_{||}\mathbf{b_0} + v_{||}\frac{\overline{\boldsymbol{\delta}\mathbf{B}}}{B^*_{||}} + \overline{\mathbf{V}}_{\mathbf{E}} + \mathbf{v_d}, \tag{2}$$

$$\dot{v}_{||} = -\frac{1}{m_\alpha}\frac{\mathbf{B}^*}{B^*_{||}}\cdot\left(Z_\alpha\nabla\overline{\delta\phi} + \mu\nabla B_0\right) - \frac{Z_\alpha}{\mathrm{cm}_\alpha}\frac{\partial\overline{\delta A}_{||}}{\partial t}, \tag{3}$$

where Z_α, m_α and f_α represent the charge, mass and distribution for $\alpha = i, e, h$ species respectively. $\delta\phi$ and $\delta A_{||}$ are the perturbed electrostatic potential and perturbed parallel vector field of the magnetic field. $\mathbf{B}^* = \mathbf{B}^*_\mathbf{0} + \overline{\boldsymbol{\delta}\mathbf{B}}$, $\overline{\boldsymbol{\delta}\mathbf{B}} = \nabla\times\left(\overline{\delta A}_{||}\mathbf{b_0}\right)$, $\mathbf{B}^*_\mathbf{0} = \mathbf{B_0} + \left(B_0 v_{||}/\Omega_\alpha\right)\nabla\times\mathbf{b_0}$, $\Omega_\alpha = \frac{Z_\alpha B_0}{cm_\alpha}$ and $B^*_{||} = \mathbf{b_0}\cdot\mathbf{B}^*_\mathbf{0}$. The overbar $\overline{(\ldots)} = \frac{1}{2\pi}\int \mathbf{dx}d\xi\,(\ldots)\delta(\mathbf{R} + \boldsymbol{\rho}_{\boldsymbol{\alpha}} - \mathbf{x})$ represents the gyroaverage operation, ξ is the gyrophase angle, $\mathbf{x}$ is the particle position and $\boldsymbol{\rho}_{\boldsymbol{\alpha}} = \frac{\mathbf{b_0}\times\mathbf{v}_\perp}{\Omega_\alpha}$ is the gyroradius. $\overline{\mathbf{V}}_E$ and $\mathbf{v_d}$ represent the $\mathbf{E}\times\mathbf{B}$ and magnetic drift as

$$\overline{\mathbf{V}}_{\mathbf{E}} = \frac{c\mathbf{b_0}\times\nabla\overline{\delta\phi}}{B^*_{||}}$$

and

$$\mathbf{v_d} = \frac{cm_\alpha v^2_{||}}{Z_\alpha B^*_{||}}\mathbf{b_0}\times\boldsymbol{\kappa} + \frac{c\mu}{Z_\alpha B^*_{||}}\mathbf{b_0}\times\nabla B_0,$$

where the magnetic field curvature $\boldsymbol{\kappa} = \mathbf{b_0}\cdot\nabla\mathbf{b_0}$.

To reduce particle noise, the δf-method is used to solve equations (1)–(3), splitting the propagator and distribution function into equilibrium and perturbed parts as $L = L_0 + \delta L$ and $f_\alpha = f_{\alpha 0} + \delta f_\alpha$, and reading

$$L_0 = \frac{\partial}{\partial t} + \left(v_{||}\mathbf{b_0} + \mathbf{v_d}\right)\cdot\nabla - \frac{\mu}{m_\alpha B^*_{||}}\mathbf{B}^*_\mathbf{0}\cdot\nabla B_0\frac{\partial}{\partial v_{||}},$$

$$\delta L = \left(\overline{\mathbf{V}}_E + v_{||}\frac{\overline{\boldsymbol{\delta}\mathbf{B}}}{B^*_{||}}\right)\cdot\nabla - \left[\frac{\mu}{m_\alpha B^*_{||}}\overline{\boldsymbol{\delta}\mathbf{B}}\cdot\nabla B_0 + \frac{Z_\alpha}{m_\alpha}\left(\frac{\mathbf{B}^*}{B^*_{||}}\cdot\nabla\overline{\delta\phi} + \frac{1}{c}\frac{\partial\overline{\delta A}_{||}}{\partial t}\right)\right]\frac{\partial}{\partial v_{||}}.$$

The equilibrium distribution function can be approximated using the local Maxwellian as $f_{\alpha 0} = n_{\alpha 0}(\frac{m_\alpha}{2\pi T_{\alpha 0}})^{3/2}\exp(-\frac{m_\alpha v^2_{||} + 2\mu B_0}{2T_{\alpha 0}})$, where $n_{\alpha 0}$ is the equilibrium density and $T_{\alpha 0}$ is the equilibrium temperature of each species. Then equations (1)–(3) can be decomposed into separate equations for $f_{\alpha 0}$ and δf_α as

$$L_0 f_{\alpha 0} = 0 \tag{4}$$

and

$$\left(L_0 + \delta L\right)\delta f_\alpha = -\delta L f_{\alpha 0}. \tag{5}$$

Then we only need to evaluate δf_α from equation (5) using gyrokinetic particle simulation and greatly decrease the particle noise level from the equilibrium part. In practice with the δf-method an equivalent particle weight equation is evolved for $w_\alpha = \delta f_\alpha / f_\alpha$ instead of equation (5), which reads

$$\frac{\mathrm{d}w_\alpha}{\mathrm{d}t} = (1-w_\alpha)\left[-\left(v_{||}\frac{\overline{\boldsymbol{\delta B}}}{B^*_{||}}+\overline{\mathbf{V}}_{\mathbf{E}}\right)\cdot\frac{\nabla f_{\alpha 0}}{f_\alpha}+\frac{1}{m_\alpha}\left(Z_\alpha\frac{\mathbf{B}^*}{B^*_{||}}\cdot\nabla\overline{\delta\phi}+\frac{Z_\alpha}{c}\frac{\partial\overline{\delta A}_{||}}{\partial t}+\mu\frac{\overline{\boldsymbol{\delta B}}}{B^*_{||}}\cdot\nabla B_0\right)\frac{1}{f_{\alpha 0}}\frac{\partial f_{\alpha 0}}{\partial v_{||}}\right]. \tag{6}$$

Next, we present the massless fluid equations for electrons with Maxwellian equilibrium distribution $f_{e0} = n_{e0}(\frac{m_e}{2\pi T_{e0}})^{3/2}\exp(-\frac{m_e v_{||}^2+2\mu B_0}{2T_{e0}})$. Applying equation (5) for electron species and integrating in velocity space, we can obtain the electron continuity equation for time advancing perturbed electron density δn_e as

$$\frac{\partial\delta n_e}{\partial t}+\nabla\cdot\left[n_{e0}\left(\delta u_{||e}\mathbf{b_0}+\mathbf{V_E}+u_{||e0}\frac{\boldsymbol{\delta B}}{B_0}\right)+\frac{1}{T_{e0}}\left(\delta P_{\perp e}\mathbf{V_g}+\delta P_{||e}\mathbf{V_c}\right)\right]=0, \tag{7}$$

where $\delta u_{||e}$ and $u_{||e0}$ are the perturbed and equilibrium parallel velocities and $\mathbf{V_g} = \frac{cT_{e0}}{q_e B_0^2}\mathbf{b_0}\times\nabla B_0$, $\mathbf{V_c} = \frac{cT_{e0}}{q_e B_0}\mathbf{b_0}\times\boldsymbol{\kappa}$. $\delta P_{||e} = \int m_e v_{||}^2 \delta f_e \mathbf{dv}$ is perturbed parallel pressure, $\delta P_{\perp e} = \int \mu B_0 \delta f_e \mathbf{dv}$ is perturbed perpendicular pressure, and $\int \mathbf{dv} = \frac{2\pi}{m_e}\int B^*_{||}\mathrm{d}v_{||}\mathrm{d}\mu$. The electron parallel fluid velocity $\delta u_{||e}$ can be calculated by inverting the parallel Ampère's law as

$$\delta u_{||e} = \frac{Z_i n_{i0}}{e n_{e0}}\overline{\delta u}_{||i}+\frac{Z_h n_{h0}}{e n_{e0}}\overline{\delta u}_{||h}+\frac{c}{4\pi e n_{e0}}\nabla_\perp^2\overline{\delta A}_{||}, \tag{8}$$

where $n_{i0}\overline{\delta u}_{||i} = \int v_{||}\delta f_i \mathbf{dv}$, $n_{h0}\overline{\delta u}_{||h} = \int v_{||}\delta f_h \mathbf{dv}$, and $\int \mathbf{dv} = \frac{2\pi}{m_\alpha}\int B^*_{||}\mathrm{d}v_{||}\mathrm{d}\mu\frac{1}{2\pi}\int\delta(\mathbf{R}+\boldsymbol{\rho_\alpha}-\mathbf{x})\mathbf{dR}\mathrm{d}\xi$. To the lowest-order adiabatic electron response, we have

$$v_{||}\mathbf{b_0}\cdot\nabla\delta f_e = -v_{||}\frac{\boldsymbol{\delta B}}{B_0}\cdot\nabla f_{e0}-\left[\frac{\mu}{B_0}\boldsymbol{\delta B}\cdot\nabla B_0+q_e\left(\mathbf{b_0}\cdot\nabla\delta\phi+\frac{1}{c}\frac{\partial\delta A_{||}}{\partial t}\right)\right]\frac{v_{||}}{T_{e0}}f_{e0}. \tag{9}$$

For most pressure-driven Alfvénic modes, the parallel vector potential is dominated by the non-tearing component $\delta A_{||}\approx\delta A_{||}\left(k_{||}\neq 0\right)$, and $\partial\delta A_{||}/\partial t$ can be expressed as

$$\frac{\partial\delta A_{||}}{\partial t} = c\mathbf{b_0}\cdot\nabla\delta\phi_{\mathrm{ind}}. \tag{10}$$

Considering equation (10) and the definitions of $\boldsymbol{\delta B} = \nabla\times\left(\delta A_{||}\mathbf{b_0}\right)$, $\mathbf{B_0} = \nabla\psi_{p0}\times\nabla\alpha_0$ and $\boldsymbol{\delta B} = \nabla\psi_{p0}\times\nabla\delta\alpha+\nabla\delta\psi_p\times\nabla\alpha_0$ using Clebsch representation in Boozer magnetic flux coordinates, with ψ_{p0} and $\delta\psi_p$ being the equilibrium and perturbed poloidal magnetic fluxes, one can solve δf_e from equations (9) and (10) as

$$\delta f_e = \frac{e}{T_{e0}}(\delta\phi+\delta\phi_{\mathrm{ind}})f_{e0}+\frac{\partial f_{e0}}{\partial\psi_{p0}}\Big|_{v_{||},v_\perp}\delta\psi_p+\frac{\partial f_{e0}}{\partial\alpha_0}\Big|_{v_{||},v_\perp}\delta\alpha, \tag{11}$$

where the dynamics equations for $\delta\psi_p$ and $\delta\alpha$ can be obtained as

$$\frac{\partial\delta\psi_p}{\partial t} = -c\frac{\partial\delta\phi_{\mathrm{ind}}}{\partial\alpha_0}, \tag{12}$$

and

$$\frac{\partial\delta\alpha}{\partial t} = c\frac{\partial\delta\phi_{\mathrm{ind}}}{\partial\psi_{p0}}. \tag{13}$$

Integrating equation (11) in velocity space, we can obtain the equation for evaluating $\delta\phi_{\mathrm{ind}}$ as

$$\frac{e\delta\phi_{\mathrm{ind}}}{T_{e0}} = \frac{\delta n_e}{n_{e0}}-\frac{e\delta\phi}{T_{e0}}-\frac{1}{n_{e0}}\frac{\partial n_{e0}}{\partial\psi_{p0}}\delta\psi_p-\frac{1}{n_{e0}}\frac{\partial n_{e0}}{\partial\alpha_0}\delta\alpha \tag{14}$$

and adiabatic electron pressure moments $\delta P_{||e}$ and $\delta P_{\perp e}$

$$\delta P_{||e} = \delta P_{\perp e} = e n_{e0}(\delta\phi+\delta\phi_{\mathrm{ind}})+\frac{\partial(n_{e0}T_{e0})}{\partial\psi_{p0}}\delta\psi_p+\frac{\partial(n_{e0}T_{e0})}{\partial\alpha_0}\delta\alpha. \tag{15}$$

$\delta\phi$ is solved by the quasi-neutrality condition

$$\sum_{\alpha=i,h}\frac{Z_\alpha^2 n_{\alpha 0}}{T_{\alpha 0}}\left(\delta\phi-\widetilde{\delta\phi}_\alpha\right) = Z_i\overline{\delta n}_i+Z_h\overline{\delta n}_h-e\delta n_e, \tag{16}$$

where $\widetilde{\delta\phi}_\alpha = \frac{1}{n_{\alpha 0}}\int f_{\alpha 0}\overline{\delta\phi}\mathbf{dv}$ is the second gyrophase-averaged potential and $\overline{\delta n}_\alpha = \int\delta f_\alpha \mathrm{d}\mathbf{v}$. Equations (1)–(3), (6)–(8), (10) and (14)–(16) form a closed system for the gyrokinetic thermal ion/EI and massless fluid electron electromagnetic simulation model. Specifically, EI model A consists of equations (1)–(3) and (6), and applies the conventional δf-method to solve δf_h directly and does not differentiate adiabatic fluid convection and non-adiabatic kinetic responses.

2.2. EI model B: split adiabatic fluid convection and non-adiabatic kinetic responses using the Chen–Hasegawa scheme

In order to investigate the different roles of EI fluid and kinetic effects on KBM instability, we further split the EI gyrocenter perturbed distribution into adiabatic and non-adiabatic parts as $\delta f_h = \delta f_h^A + \delta K_h$ following kinetic theory [11, 20, 28]. According to the Chen–Hasegawa scheme [20], the gyrocenter adiabatic distribution δf_h^A in $(\mathbf{R},\varepsilon,\mu)$ space is defined as

$$\delta f_h^A = \frac{Z_h}{m_h}\frac{\partial f_{h0}}{\partial\varepsilon}J_0\delta\phi-\frac{Z_h}{m_h}\frac{1}{\omega}\hat{Q}f_{h0}J_0\delta\psi, \tag{17}$$

where $\varepsilon = v^2/2$ is the energy per unit mass, $\hat{Q}f_{h0} = \omega\frac{\partial f_{h0}}{\partial\varepsilon} + \frac{1}{\Omega_h}\mathbf{k}\times\mathbf{b_0}\cdot\nabla f_{h0}|_{\varepsilon,\mu}$, $\Omega_h = \frac{Z_h B_0}{cm_h}$, $J_0 = J_0(k_\perp\rho_h)$ is the zeroth Bessel function of the first kind and $\rho_h = v_\perp/\Omega_h$ is the Larmor radius. The perturbed field $\delta\psi$ is related to the parallel vector potential $\delta A_{||}$ through $\frac{\partial\delta A_{||}}{\partial t} = -c\mathbf{b_0}\cdot\nabla\delta\psi$. Then the linear gyrokinetic equation for the gyrocenter non-adiabatic distribution δK_h is

$$\begin{aligned}&\frac{\partial\delta K_h}{\partial t} + \left(v_{||}\mathbf{b_0} + \mathbf{v_d}\right)\cdot\nabla\delta K_h|_{\varepsilon,\mu}\\ &= i\frac{Z_h}{m_h}\hat{Q}f_{h0}\left(J_0\delta\phi - J_0\delta\psi\right) + \frac{Z_h}{m_h}\frac{1}{\omega}\hat{Q}f_{h0}\mathbf{v_d}\cdot\nabla\left(J_0\delta\psi\right).\end{aligned} \tag{18}$$

Note that the nonlinear terms have been removed in equation (18). The linear gyrokinetic vorticity equation can be obtained by integrating equations (17) and (18) in energy space considering the parallel Ampère's law equation (8) and quasi-neutrality condition equation (16), which reads

$$\begin{aligned}&\frac{\omega^2}{V_A^2}\left(\frac{n_{i0}}{n_{e0}} + \frac{n_{h0}m_h}{n_{e0}m_i}\right)\nabla_\perp^2\overline{\delta\phi}\\ &\underbrace{-\frac{\omega}{V_A^2}\left(\frac{n_{i0}}{n_{e0}}\omega_{*p,i} + \frac{n_{h0}m_h}{n_{e0}m_i}\omega_{*p,h}\right)\nabla_\perp^2\overline{\delta\phi}}_{\text{term}\{A\}}\\ &+\mathbf{B_0}\cdot\nabla\left[\frac{1}{B_0}\nabla_\perp^2\left(\mathbf{b_0}\cdot\nabla\overline{\delta\psi}\right)\right]\\ &-\frac{4\pi}{c}\nabla\left(\mathbf{b_0}\cdot\nabla\overline{\delta\psi}\right)\times\mathbf{b_0}\cdot\nabla\left(\frac{J_{||0}}{B_0}\right)\\ &\underbrace{-\frac{4\pi\,i\omega}{c^2}\sum_{\alpha=i,e,h}c\frac{\mathbf{b_0}\times\boldsymbol{\kappa}}{B_0}\cdot\nabla\left(\overline{\delta P}^A_{||\alpha} + \overline{\delta P}^A_{\perp\alpha}\right)}_{\text{term}\{B\}}\\ &\underbrace{-\frac{4\pi\,i\omega}{c^2}\sum_{\alpha=i,e,h}Z_\alpha\langle J_0\mathbf{v_d}\cdot\nabla\delta K_\alpha\rangle_{v,\alpha}}_{\text{term}\{C\}} = 0,\end{aligned} \tag{19}$$

where $\omega_{*p,\alpha} = \frac{cT_{\alpha0}}{Z_\alpha B_0}\mathbf{k}\times\mathbf{b_0}\cdot\frac{\nabla P_{\alpha0}}{n_{\alpha0}T_{\alpha0}}, \alpha = i,h$ are the diamagnetic drift frequencies of thermal ions and EIs, respectively, and $V_A = \frac{B_0}{\sqrt{4\pi n_{e0}m_i}}$, $\langle\ldots\rangle_{v,\alpha} = \int(\ldots)\frac{2\pi}{m_\alpha}B^*_{||}\mathrm{d}v_{||}\mathrm{d}\mu\delta(\mathbf{R} + \boldsymbol{\rho_\alpha} - \mathbf{x})\mathbf{dR}d\xi/(2\pi)$. $\overline{\delta P}^A_{||\alpha} = \langle m_\alpha v_{||}^2\delta f^A_\alpha\rangle_{v,\alpha}$ and $\overline{\delta P}^A_{\perp\alpha} = \langle\mu B_0\delta f^A_\alpha\rangle_{v,\alpha}$ represent the adiabatic pressure moments. Term $\{A\}$ represents the plasma diamagnetic convection induced by thermal ion FLR and EI FLR, terms $\{B\}$ and $\{C\}$ represent MHD ballooning-interchange and the KPC from all species, respectively.

Next, we shall construct EI model B in the GTC initial value simulation, consistent with the theoretical model of equations (17)–(19). For Maxwellian equilibrium $f_{h0} = n_{h0}\left(\frac{m_h}{2\pi T_{h0}}\right)^{3/2}\exp\left(-\frac{m_h\varepsilon}{T_{h0}}\right)$, equation (17) can be explicitly written as

$$\begin{aligned}\delta f_h^A = &-\frac{Z_h}{T_{h0}}J_0\left(\delta\phi - \delta\psi\right)f_{h0} - \frac{Z_h}{T_{h0}}J_0\delta\psi\frac{\omega_{*n,h}}{\omega}\\ &\times\left[1 + \eta_h\left(\frac{m_h\varepsilon}{T_{h0}} - \frac{3}{2}\right)\right]f_{h0},\end{aligned} \tag{20}$$

where $\eta_h = \nabla T_{h0}/\nabla n_{h0}$. Considering the relation $\nabla f_{h0}|_{v_{||},\mu} = \nabla f_{h0}|_\varepsilon - \frac{\mu\nabla B_0}{T_{h0}}f_{h0}$ that is valid for isotropic Maxwellian equilibrium, it is straightforward to prove that equation (20) is consistent with the following adiabatic response equation in GTC $\left(\mathbf{R}, v_{||}, \mu\right)$ coordinates:

$$\begin{aligned}v_{||}\mathbf{b_0}\cdot\nabla\delta f_h^A = &-v_{||}\frac{\overline{\boldsymbol{\delta}\mathbf{B}}}{B_0}\cdot\nabla f_{h0}|_{v_{||},\mu} - \left[\frac{\mu}{B_0}\overline{\boldsymbol{\delta}\mathbf{B}}\right.\\ &\left.\cdot\nabla B_0 + Z_h\left(\mathbf{b_0}\cdot\nabla\overline{\delta\phi} + \frac{1}{c}\frac{\partial\overline{\delta A}_{||}}{\partial t}\right)\right]\frac{v_{||}}{T_{h0}}f_{h0}.\end{aligned} \tag{21}$$

Since the form of equation (20) explicitly contains ω that leads to difficulty for initial value simulation, we solve equation (21) using the same method as the adiabatic electron response in section 2.1, the solution of which reads

$$\delta f_h^A = -\frac{Z_h}{T_{h0}}\left(\overline{\delta\phi} + \overline{\delta\phi}_{\text{ind}}\right)f_{h0} + \frac{\partial f_{h0}}{\partial\psi_{p0}}\Big|_{v_\perp}\overline{\delta\psi}_p + \frac{\partial f_{h0}}{\partial\alpha_0}\Big|_{v_\perp}\overline{\delta\alpha}, \tag{22}$$

where

$$\frac{\partial\overline{\delta\psi}_p}{\partial t} = -c\frac{\partial\overline{\delta\phi}_{\text{ind}}}{\partial\alpha_0} \tag{23}$$

and

$$\frac{\partial\overline{\delta\alpha}}{\partial t} = c\frac{\partial\overline{\delta\phi}_{\text{ind}}}{\partial\psi_{p0}}. \tag{24}$$

Substituting equation (22) into equation (5), the linearized equation for the EI non-adiabatic kinetic response δK_h in GTC simulation coordinates is

$$\begin{aligned}&\left[\frac{\partial}{\partial t} + \left(v_{||}\mathbf{b_0} + \mathbf{v_d}\right)\cdot\nabla|_{v_{||},\mu} - \frac{\mu}{m_h B_0}\mathbf{B_0^*}\cdot\nabla B_0\frac{\partial}{\partial v_{||}}\right]\delta K_h\\ &= -\left(v_{||}\frac{\overline{\boldsymbol{\delta}\mathbf{B}}}{B_0} + \overline{\mathbf{v}}_\mathbf{E}\right)\cdot\nabla f_{h0}|_{v_{||},\mu} + \left[\frac{\mu}{m_h B_0}\overline{\boldsymbol{\delta}\mathbf{B}}\cdot\nabla B_0 + \frac{Z_h}{m_h}\right.\\ &\quad\left.\times\left(\frac{\mathbf{B_0^*}}{B_0}\cdot\nabla\overline{\delta\phi} + \frac{1}{c}\frac{\partial\overline{\delta A}_{||}}{\partial t}\right)\right]\frac{\partial f_{h0}}{\partial v_{||}}\\ &\quad - \left[\frac{\partial}{\partial t} + \left(v_{||}\mathbf{b_0} + \mathbf{v_d}\right)\cdot\nabla|_{v_{||},\mu} - \frac{\mu}{m_h B_0}\mathbf{B_0^*}\cdot\nabla B_0\frac{\partial}{\partial v_{||}}\right]\delta f_h^A.\end{aligned} \tag{25}$$

By performing coordinate transform between $\left(\mathbf{R}, v_{||}, \mu\right)$ and $(\mathbf{R}, \varepsilon, \mu)$, it is straightforward to show that equation (25) is identical to equation (18) for the isotropic Maxwellian equilibrium case. Integrating equation (5) for EI species in velocity space, keeping the linear terms and considering the $\delta B_{||}$ effect of drift reversal cancellation by replacing $\nabla B_0/B_0$ with $\boldsymbol{\kappa}$ [18], we have

$$\frac{\partial\overline{\delta n_h}}{\partial t}+\mathbf{B_0}\cdot\nabla\left(\frac{n_{h0}\overline{\delta u}_{||h}}{B_0}\right)$$
$$\underbrace{+\int\frac{c}{B_0}\left(\mathbf{b_0}\times\nabla\overline{\delta\phi}\cdot\nabla\ln f_{h0}|_{v_{||},\mu}+\nabla\times\mathbf{b_0}\cdot\nabla\overline{\delta\phi}\right)f_{h0}\mathbf{dv}}_{\text{term}\{D\}}$$
$$\underbrace{+\frac{c}{Z_h}\frac{\mathbf{b_0}\times\boldsymbol{\kappa}}{B_0}\cdot\nabla\left(\overline{\delta P}^A_{||h}+\overline{\delta P}^A_{\perp h}\right)}_{\text{term}\{E\}}$$
$$\underbrace{+\frac{c}{Z_h}\frac{\mathbf{b_0}\times\boldsymbol{\kappa}}{B_0}\cdot\nabla\left(\overline{\delta P}^{NA}_{||h}+\overline{\delta P}^{NA}_{\perp h}\right)}_{\text{term}\{F\}}=0, \tag{26}$$

where

$$\overline{\delta u}_{||h}=\frac{1}{n_{h0}}\int v_{||}\delta K_h\mathbf{dv}, \tag{27}$$
$$\overline{\delta P}^A_{||h}=\int m_h v_{||}^2\delta f_h^A\mathbf{dv}=-Z_h n_{h0}\left(\widetilde{\delta\phi}+\widetilde{\delta\phi}_{\text{ind}}\right)+\frac{\partial\left(n_{h0}T_{h0}\right)}{\partial\psi_{p0}}\widetilde{\delta\psi}_p+\frac{\partial\left(n_{h0}T_{h0}\right)}{\partial\alpha_0}\widetilde{\delta\alpha}, \tag{28}$$
$$\overline{\delta P}^A_{\perp h}=\int\mu B_0\delta f_h^A\mathbf{dv}=-Z_h n_{h0}\left(\widetilde{\delta\phi}+\widetilde{\delta\phi}_{\text{ind}}\right)+\frac{\partial\left(n_{h0}T_{h0}\right)}{\partial\psi_{p0}}\widetilde{\delta\psi}_p+\frac{\partial\left(n_{h0}T_{h0}\right)}{\partial\alpha_0}\widetilde{\delta\alpha}, \tag{29}$$
$$\overline{\delta P}^{NA}_{||h}=\int m_h v_{||}^2\delta K_h\mathbf{dv} \tag{30}$$

and

$$\overline{\delta P}^{NA}_{\perp h}=\int\mu B_0\delta K_h\mathbf{dv}. \tag{31}$$

It should be noted that terms $\{D\}$, $\{E\}$ and $\{F\}$ in equation (26) corresponds to terms $\{A\}$, $\{B\}$ and $\{C\}$ in equation (19), and represent EI-induced plasma diamagnetic convection, MHD ballooning-interchange and KPC, respectively.

Making use of equations (7), (14) and (23), the time derivative term $\partial_t\delta f_h^A$ on the right-hand side of equation (25) can be evaluated by

$$\frac{1}{f_{h0}}\frac{\partial\delta f_h^A}{\partial t}=-\frac{Z_h}{e}\frac{T_{e0}}{T_{h0}}\frac{1}{n_{e0}}\frac{\partial\overline{\delta n}_e}{\partial t}+\left(\frac{\partial\ln f_{h0}}{\partial\psi_{p0}}\Big|_\varepsilon+\frac{Z_h}{e}\frac{T_{e0}}{T_{h0}}\frac{\partial\ln n_{e0}}{\partial\psi_{p0}}\right)\left(-c\frac{\partial\overline{\delta\phi}_{\text{ind}}}{\partial\alpha_0}\right). \tag{32}$$

Equations (22) and (32) form EI model B that connects the GTC conventional EI model A in section 2.1 [25] and the theoretical model described by equations (17)–(19) [20], which enables us to clarify the importance of different physical factors and reveal the underlying mechanisms of EI–KBM interactions in different EI energy and pitch angle regimes.

3. Simulation results

There are two main routes for EIs to affect KBM stability. The first is via increased plasma pressure, which enhances the Shafranov shift through equilibrium force balance that stabilizes ballooning modes in the second stability region. The second is via modification of the dispersive properties of the KBM through the contributions of EIs to the plasma dielectric tensor. This work focuses on the second route to reveal EI–KBM interaction mechanisms, based on linear and nonlinear GTC simulations covering a broad range of EI pressure ratios, orbit widths and characteristic frequencies. To identify the crucial roles of EI fluid and kinetic effects on KBM stability, both EI model A using the conventional δf-method and EI model B using the split scheme are applied in this section, and detailed information on EI total response δf_h, adiabatic fluid response δf_h^A and non-adiabatic kinetic response δK_h, as well as corresponding pressure perturbation structures, is provided. It is worthwhile mentioning that the effect of EIs on the KBM can be either perturbative or non-perturbative. In the perturbative regime, the KBM growth rate and real frequency are weakly modified by EIs with small variations $\Delta\gamma\ll\gamma_0$ and $\Delta\omega_r\ll\omega_0$. In the non-perturbative regime, the EI-induced growth rate and real frequency variations increase to $\Delta\gamma\sim\gamma_0$ and $\Delta\omega_r\sim\omega_0$, and the spatial mode structure is also influenced by the EI drive profile. Here, γ_0 and ω_0 denote the KBM growth rate and real frequency in a single-ion-species plasma without EIs.

To clarify the general physical process of EI–KBM interaction and keep the geometric complexity at a minimum, a model equilibrium with concentric circular geometry is applied in the simulations based on Cyclone Base Case (CBC) parameters. The magnetic field geometry parameters include the major radius $R_0=83.5$ cm, the inverse aspect ratio $a/R_0=0.357$, the safety factor $q=1.4$ and magnetic shear $s=(r/q)(dq/dr)=0.78$ at $r=0.5a$, and the on-axis magnetic field strength $B_a=2.01$ T. The background plasma parameters include $T_i=T_e=2223$ eV, $\rho_i/R_0\approx0.0029$, $R_0/L_{T,i}=R_0/L_{T,e}=6.9$, $n_e=9\times10^{13}\,\text{cm}^{-3}$, $R_0/L_{n,e}=2.2$ and $\beta_e=2\%$ at location $q=1.4$, where $L_{T,e}=|\nabla T_e/T_e|^{-1}$, $L_{T,i}=|\nabla T_i/T_i|^{-1}$ and $L_{n,e}=|\nabla n_e/n_e|^{-1}$. The EI density $n_h=0.03n_e$ and $R_0/L_{n,h}=20$ at location $q=1.4$, where $L_{n,h}=|\nabla n_h/n_h|^{-1}$. The EI temperature T_h is uniform (i.e. $R_0/L_{T,h}=0$) and varies in different cases. The thermal ion density is determined by the quasi-neutrality condition $Z_i n_i=en_e-Z_h n_h$ and the proton charge is applied for both thermal ions and EI species (i.e. $Z_i=Z_h=e$). Within these parameters, the reference case of a $n=10$ KBM in two-species plasmas without EIs gives a real frequency of $\omega_0=2.17C_s/R_0$ and growth rate of $\gamma_0=1.42C_s/R_0$, where $C_s=\sqrt{T_e/m_i}$ is the speed of sound.

In present-day tokamaks and future fusion reactors, EIs are characterized by a small density with $n_h\ll n_{e,i}$ and a high energy with $T_h\gg T_{e,i}$, which result in the same order of pressure magnitude for EI and thermal species as $\beta_h\sim\beta_{e,i}$; thus EIs can become non-trivial for electromagnetic Alfvénic modes with a free energy drive scaled by pressure, including MHD ballooning-interchange and KPC and being comparable with bulk plasmas [3], namely, terms $\{B\}$ and

Table 1. The EI dimensionless parameters at $T_h/T_e = 3$ and $T_h/T_e = 25$. $\omega_\phi = v_{\rm th}/R_0$ and $\omega_\theta = v_{\rm th}/(qR_0)$ denote the passing EI toroidal and poloidal frequencies at thermal speed. $\omega_b = \sqrt{\epsilon}v_{\rm th}/(qR_0)$ and $\omega_{\rm pre} = qE_h/(rm_hR_0\Omega_h)$ denote the trapped EI bounce frequency at thermal speed and precession frequency at $E_h = T_h$, where $v_{\rm th} = \sqrt{T_h/m_h}$, $\epsilon = r/R_0$, $\Omega_h = Z_hB_a/{\rm cm}_h$ and ω_0 denotes the real KBM frequency in two-species plasmas without EI. The resonance conditions of passing and trapped EIs can be expressed as $\omega = n\omega_\phi - p\omega_\theta$ and $\omega = n\omega_{\rm pre} + l\omega_b$, respectively, where p and l are integers. $\rho_h = v_{\rm th}/\Omega_h$, $\rho_d^p = q\rho_h$ and $\rho_d^t = q\rho_h/\sqrt{\epsilon}$ represent the EI FLR, passing EI FOW and trapped EI FOW, respectively. All are normalized by KBM poloidal wave vector k_θ.

Case	m_h/m_p	T_h/T_e	β_h	ω_ϕ/ω_0	ω_θ/ω_0	ω_b/ω_0	$n\omega_{\rm pre}/\omega_0$	$k_\theta\rho_h$	$k_\theta\rho_d^p$	$k_\theta\rho_d^t$
(I)	1	3	$0.09\beta_e$	1.13	0.81	0.34	0.76	0.55	0.78	1.8
(I)	1	25	$0.75\beta_e$	3.26	2.33	0.98	6.3	1.6	2.2	5.3
(II)	0.01	3	$0.09\beta_e$	11.3	8.1	3.4	0.76	0.055	0.078	0.18
(II)	0.01	25	$0.75\beta_e$	32.6	23.3	9.8	6.3	0.16	0.22	0.53

$\{C\}$ in equation (19) or equivalently terms $\{E\}$ and $\{F\}$ in equation (26). For comparison, EIs have a weak impact on electrostatic modes with free energy drive scaled by density, which is much smaller than for bulk plasmas with $n_h \ll n_{e,i}$ [7]. The physical processes of EI–KBM interaction are primarily determined by the normalized temporal and spatial scales of EI motion in terms of KBM frequency and wavelength, which are associated with wave–particle resonance and orbit averaging. Considering these facts, we focus on three dimensionless parameters, the EI–thermal electron temperature ratio T_h/T_e, the KBM perpendicular wave vector normalized by EI orbit width $k_\theta\rho_d$ (i.e. FOW) and the EI pressure ratio β_h, and explain the roles of EI fluid and kinetic effects on KBM stability in different regimes. In practice, we choose a $n = 10$ KBM for all simulations, which has been well tested in two-species bulk plasmas [18, 19], and vary T_h/T_e and m_h/m_p for combinations of different resonance channels, $k_\theta\rho_d$ and β_h regimes. Specifically, a series of simulations are conducted in two groups: case (I) applies $m_h/m_p = 1$ and case (II) applies $m_h/m_p = 0.01$; both scan T_h/T_e in the range of $T_h/T_e \in [1, 35]$, where examples are listed in table 1 for the key parameters of low temperature $T_h/T_e = 3$ and high temperature $T_h/T_e = 25$. Note that the dimensionless parameters are instructive in physics rather than the actual values used here. Case (I) using $m_h/m_p = 1$ is relevant to neutral beam injection (NBI) EIs in present-day machines of small or medium size, characterized by $E_h \sim 100$ keV, $R_0 \sim 1$ m and large dimensionless orbits (i.e. $k_\theta\rho_d \gg 1$). Case (II) using $m_h/m_p = 0.01$ increases ω_ϕ, ω_θ and ω_b by a factor of 10, decreases $k_\theta\rho_h$ and $k_\theta\rho_d$ by a factor of 10 and does not alter $\omega_{\rm pre}$, which can be analogous to the conditions of fusion-born alpha particles in large machines such as ITER, characterized by $E_h \sim 1$ MeV, $R_0 \sim 6$ m and small dimensionless orbits (i.e. $k_\theta\rho_d \ll 1$) [29].

3.1. Perturbative EI influence on the KBM in the short-wavelength regime of $k_\theta\rho_d \gg 1$

We first carry out T_h/T_e scan simulations for case (I), which covers both the helium ash parameter regimes ($\beta_h \ll \beta_{e,i}, T_h/T_e \sim 1, k_\theta\rho_d \sim 1$) and the small machine NBI EI parameter regimes ($\beta_h \sim \beta_{e,i}, T_h/T_e \gg 1, k_\theta\rho_d \gg 1$). For fixed EI density $n_h = 0.03n_e$, EI mass $m_h/m_p = 1$ and a $n = 10$ KBM, the dimensionless EI orbit frequencies and orbit widths are computed at $T_h/T_e = 3$ and $T_h/T_e = 25$ in table 1, which are relevant to helium ash and NBI EIs, respectively.

The dependences of real frequency ω_r and growth rate γ on T_h/T_e for a $n = 10$ KBM are shown in figure 1, where the results for EI models A and B show excellent agreement, demonstrating that the split scheme introduced in section 2.2 can faithfully capture the comprehensive EI physics for EI–KBM interactions. It is seen that both KBM ω_r and γ are insensitive to T_h/T_e with variations up to $\Delta\omega_r/\omega_r \sim 20\%$ and $\Delta\gamma_r/\gamma_r \sim 30\%$ across a broad range of $T_h/T_e \in [1, 35]$. As T_h/T_e increases, ω_r exhibits an increasing trend, while γ increases in the regime of $T_h/T_e \sim 1$ and decreases in the regime of $T_h/T_e \gg 1$ non-monotonically. Note that the KBM dispersion relation curves are bounded by the thermal ion limit and dilution limit, which are denoted by the green and black dotted lines in figure 1: the dilution limit keeps the EI fraction in the equilibrium quasi-neutrality condition of $Z_in_i = en_e - Z_hn_h$ while it reduces EI perturbations of $\delta n_h = 0$ and $\delta u_{||h} = 0$ in equations (8) and (16); the thermal ion limit drops for EIs in both equilibrium and perturbed parts. At $T_h/T_e = 1$, the KBM dispersion relation and mode structure are the same as the thermal ion limit results, since the properties of EIs are identical to those of the thermal ions (recall that $T_i = T_e$ for bulk plasmas). At $T_h/T_e \gg 1$, ω_r and γ curves approach the dilution limit results asymptotically, exhibiting weak stabilization compared with the thermal ion limit. The KBM mode structures of electrostatic potential $\delta\phi$ from $T_h/T_e = 1$, $T_h/T_e = 3$ and $T_h/T_e = 25$ simulations are compared in figure 2, and the $\delta A_{||}$ mode structure is correlated to $\delta\phi$ through equations (10) and (14), which is consistently modified by EIs with different T_h/T_e values and thus omitted in our analyses. In figure 2(*a*) for $T_h/T_e = 1$, the tilting angle of the two-dimensional mode structure at the outer midplane is positive in polar coordinates. For comparison, the tilting angle becomes negative in figure 2(*c*) for $T_h/T_e = 25$, which implies that the EIs still can non-perturbatively alter the KBM mode structure when $\beta_h \sim \beta_{e,i}$, despite the perturbative influence on the dispersion relation, and the specific radial profile of the EI drive determines the shape orientation of the mode structure, which will be further analyzed in detail. This phenomenon is also observed in the physical processes of EI-driven beta-induced Alfvén eigenmodes [30, 31], reversed shear Alfvén eigenmodes [32] and toroidal Alfvén eigenmodes [33]; it is also found that the radial symmetry breaking of AE mode structure can nonlinearly generate the intrinsic rotation and induce momentum transport, which is also valid for KBMs. Therefore, the overall influences of EIs in case (I)

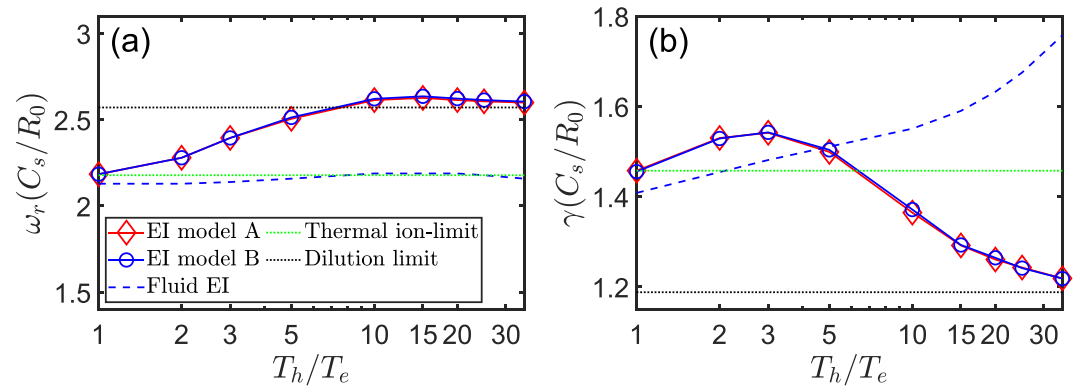

Figure 1. $n=10$ KBM dispersion relation in the presence of minor EI species with $n_h/n_e=0.03$. The dependences of KBM (a) real frequency ω_r and (b) growth rate γ on the EI–thermal electron temperature ratio T_h/T_e obtained from EI model A and EI model B. Fluid EI (blue dashed line): the remove the kinetic particle compression term $\{F\}$ in equation (26) is removed, the others are the same as EI model B. Dilution limit (black dotted line): equation (26) is removed and $\delta u_{\|h}=0$ is set in equation (8) while still keeping the EI equilibrium fraction as $Z_i n_i = e n_e - Z_h n_h$. The green dotted line denotes the thermal ion limit without EI.

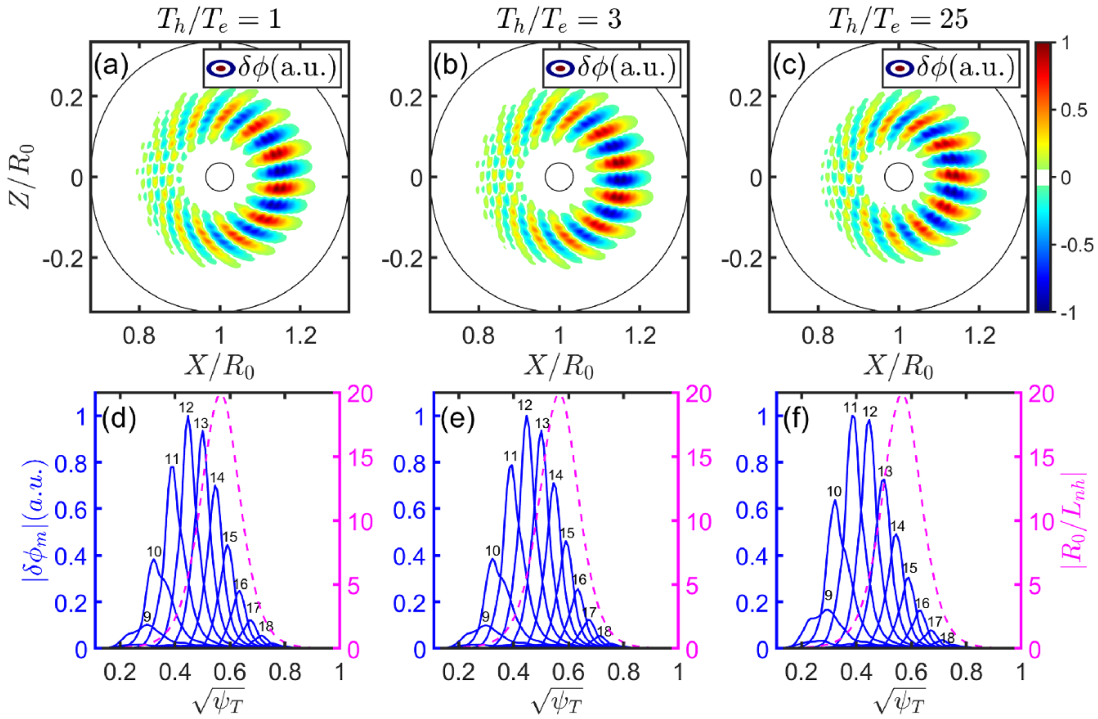

Figure 2. The 2D poloidal mode structures of electrostatic potential $\delta\phi$ (upper row) and corresponding m-harmonic radial profiles (bottom row) for a $n=10$ KBM with $T_h/T_e=1$, $T_h/T_e=3$ and $T_h/T_e=25$ from the left to right columns. The magenta lines in bottom row denote the radial profile of EI pressure gradient drive strength $|R_0/L_{n,h}|$.

are perturbative to KBMs not only in the low-temperature regime of $T_h/T_e\sim 1$ with small $\beta_h \ll \beta_{e,i}$ but also in the high-temperature regime of $T_h/T_e \gg 1$ with large $\beta_h \sim \beta_{e,i}$.

The relative strength of the EI drive can be inferred from $|\delta f_h|^2$ in (E_h,λ) phase space with $\lambda=\mu B_a/E_h$ being the pitch angle, which provides a general picture of perturbative influence of EIs in case (I). (Note that the flux surface-averaged $\langle\delta f_h\rangle=0$ for the $n>0$ component, thus we use $|\delta f_h|^2$ rather than δf_h for phase space diagnostics of the EI response to $n=10$ KBM electromagnetic fluctuations.) In figure 3, we compare the phase space structures of EI $|\delta f_h|^2$ and the full-f distribution f_h between $T_h/T_e=3$, $T_h/T_e=10$ and $T_h/T_e=25$ simulations. It is seen that the dominant part of $|\delta f_h|^2$ is distributed in the energy range $E_h/T_e\in[0,10]$, while the amplitude of f_h peaks near $E_h\sim T_h$; thus the resonant EI population $f_{\rm res}$ relies on the specific T_h/T_e ratio. For example, $|\delta f_h|^2$ distributes in the same energy range as f_h from the $T_h/T_e=3$ simulation, as shown in figures 3(a) and (d), which indicates that a large fraction of the EI population contributes to $|\delta f_h|^2$ with $f_{\rm res}\sim f_h$. In contrast, $|\delta f_h|^2$ localizes in the regime of $E_h\ll T_h$ from the $T_h/T_e=25$ simulation in figure 3(c), which corresponds to the bottom edge of f_h in figure 3(f) with $f_{\rm res}\ll f_h$. Moreover, it is noted that as T_h/T_e increases, the peak of $|\delta f_h|^2$ shifts from $E_h=2T_e$ in figure 3(a) to $E_h=6T_e$ in figure 3(c)

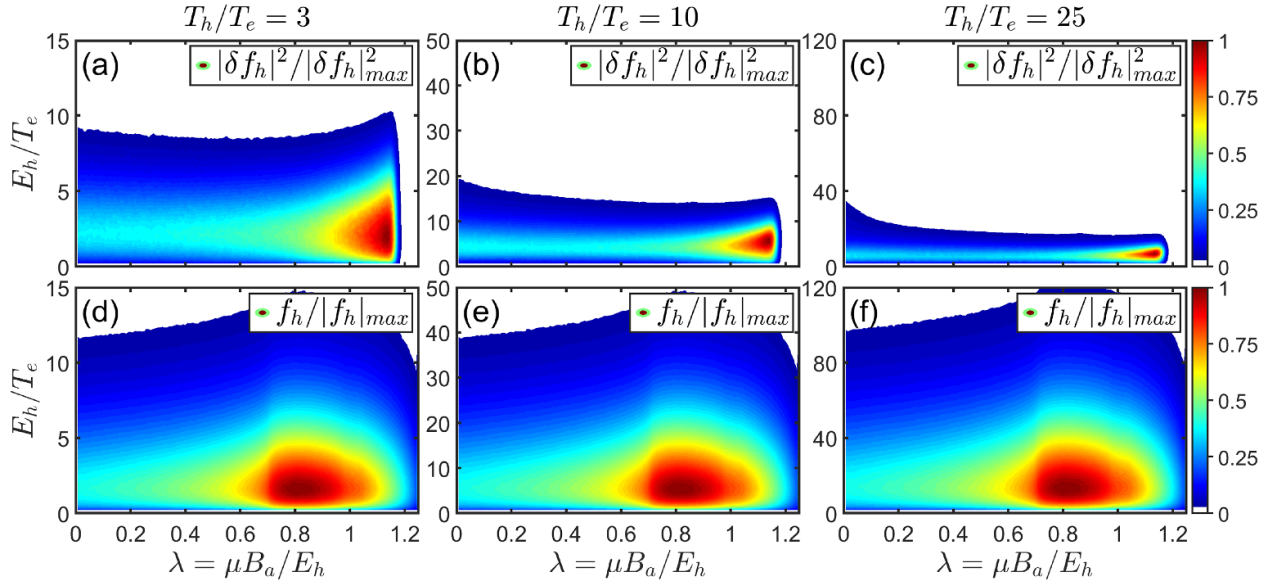

Figure 3. The phase space structures of EI-perturbed distribution intensity $|\delta f_h|^2$ and EI equilibrium distribution f_h from $n = 10$ KBM simulations with $T_h/T_e = 3$, $T_h/T_e = 10$ and $T_h/T_e = 25$ from left to right columns. The values are normalized by the maximal amplitude.

due to the energy mismatch between the dominant EI population and strong EI–KBM resonance for the $T_h/T_e = 25$ case. In addition, $|\delta f_h|^2$ peaks at $\lambda \approx 1 + \epsilon$ with $\epsilon = r/R_0$ for all T_h/T_e values, implying that deeply trapped particles dominate the EI–KBM interaction in case (I). Therefore, $\beta_h \ll \beta_{e,i}$ and $f_{\rm res} \ll f_h$ limit the EI drive strength at $T_h/T_e = 3$ and $T_h/T_e = 25$, respectively, resulting in a perturbative influence of EIs over the full T_h/T_e range in case (I). It should be pointed out that EIs are treated as minor ion species with $n_h \ll n_e$, and the variations of KBM dispersive property in figures 1 and 2 can be amplified by increasing n_h, which will lead to a non-perturbative influence on the KBM in the $n_h \sim n_i$ and $T_h \sim T_i$ regimes through the isotope effect.

The separate fluid and kinetic parts of the EI response can be evaluated from the corresponding $|\delta f|^2$-intensity and perturbed pressure, which help to elucidate in depth the underlying mechanisms of EI–KBM interaction at $T_h/T_e = 3$ and $T_h/T_e = 25$. As shown in figures 4(*a*)–(*d*) for the $T_h/T_e = 3$ simulation, the amplitudes of total δP_h, adiabatic fluid part δP_h^A and non-adiabatic kinetic part δP_h^{NA} are close to each other, and a finite poloidal phase shift exists between δP_h^A and δP_h^{NA}, which satisfies $\delta P_h = \delta P_h^A + \delta P_h^{NA}$ consistent with $\delta f_h = \delta f_h^A + \delta K_h$ as expected. Comparing figures 4(*f*) and (*g*), it is seen that $|\delta f_h^A|^2$ localizes in the deeply trapped region with a higher amplitude, while $|\delta K_h|^2$ distributes in a broader domain across the well-passing and deeply trapped regions but with a lower amplitude, of which the phase space structure domain size and amplitude complement each other, resulting in similar amplitudes of δP_h^A and δP_h^{NA} in real space. Specifically, the localization of $|\delta f_h^A|^2$ in figure 4(*f*) can be explained by equation (20): trapped particles with $\lambda > 1$ can effectively respond to the ballooning mode structure of $\delta\phi$ with large amplitude on the low-field-side, as shown in figure 2(*b*) (note that $\delta\phi \approx \delta\psi$ in the MHD limit), and the EI population density is large at $E_h \sim T_h = 3T_e$ in figure 3(*d*). Meanwhile, both transit motion resonance and precessional drift resonance are observed from the EI kinetic response intensity $|\delta K_h|^2$ in figure 4(*g*), which indicates that $\omega \sim \omega_{\rm tr} \sim n\omega_{\rm pre}$ can be well satisfied for $T_h/T_e = 3$, and the resonant EI energy of trapped species is slightly higher than that of passing species. The phase space structure of the cross term $\delta f_h^A \delta K_h$ is shown in figure 4(*h*), and its relation with $|\delta f|^2$-intensity can be expressed as

$$\delta f_h^A \delta K_h = \frac{1}{2}\left[|\delta f_h|^2 - \left(|\delta f_h^A|^2 + |\delta K_h|^2\right)\right]. \tag{33}$$

In figure 4(*h*), the positive value of $\delta f_h^A \delta K_h > 0$ in the bottom region of $E_h \sim T_e$ indicates that the EI fluid and kinetic responses accumulate together, leading to a destabilization effect on the KBM. In contrast, the negative value of $\delta f_h^A \delta K_h < 0$ in the regime of $E_h \gg T_e$ indicates that the EI fluid and kinetic responses cancel each other to a certain degree and result in a smaller net response, which is consistent with the fact that higher-energy EIs are characterized by a larger orbit width that screens more KBM electromagnetic fluctuations. In short, for the $T_h/T_e = 3$ simulation characterized by a large EI population at $E_h \sim T_e$, most EIs can effectively interact with KBMs and give comparable fluid and kinetic responses, which suffer modest FOW screening with $k_\theta \rho_d \sim 1$ and contribute to MHD ballooning-interchange (i.e. term $\{E\}$ in equation (26)) and KPC (i.e. term $\{F\}$ in equation (26)) for KBM destabilization. However, this destabilization effect by EIs with $T_h/T_e \sim 1$ is still weak in figure 1(*b*) because $\beta_h \ll \beta_{e,i}$.

The EI fluid and kinetic responses in the $T_h/T_e = 25$ simulation become qualitatively different from the $T_h/T_e = 3$ simulation. As shown in figures 5(*a*)–(*d*), the amplitude of δP_h is much smaller than its fluid component δP_h^A and kinetic component δP_h^{NA}, which are characterized by nearly opposite poloidal phases with π difference and mostly cancel each other so

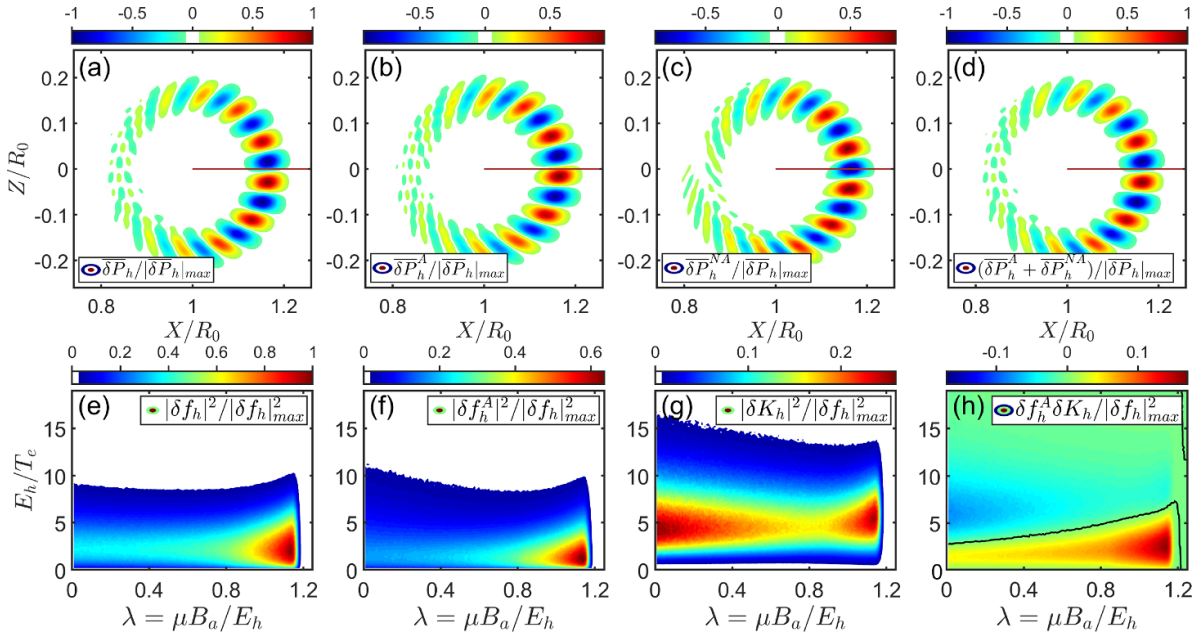

Figure 4. The 2D poloidal mode structure of EI pressure perturbations (upper row) and $|\delta f_h|^2$ intensities (bottom row) in case (I) at $T_h/T_e = 3$. Left to right columns: the normalized δP_h and $|\delta f_h|^2$ from the conventional δf-method [EI model A, adiabatic fluid part (δP_h^A and $|\delta f_h^A|^2$), non-adiabatic kinetic part (δP_h^{NA} and $|\delta K_h|^2$], sum of $\delta P_h^A + \delta P_h^{NA}$ and cross term of $\delta f_h^A \delta K_h$ from the split scheme (EI model B).

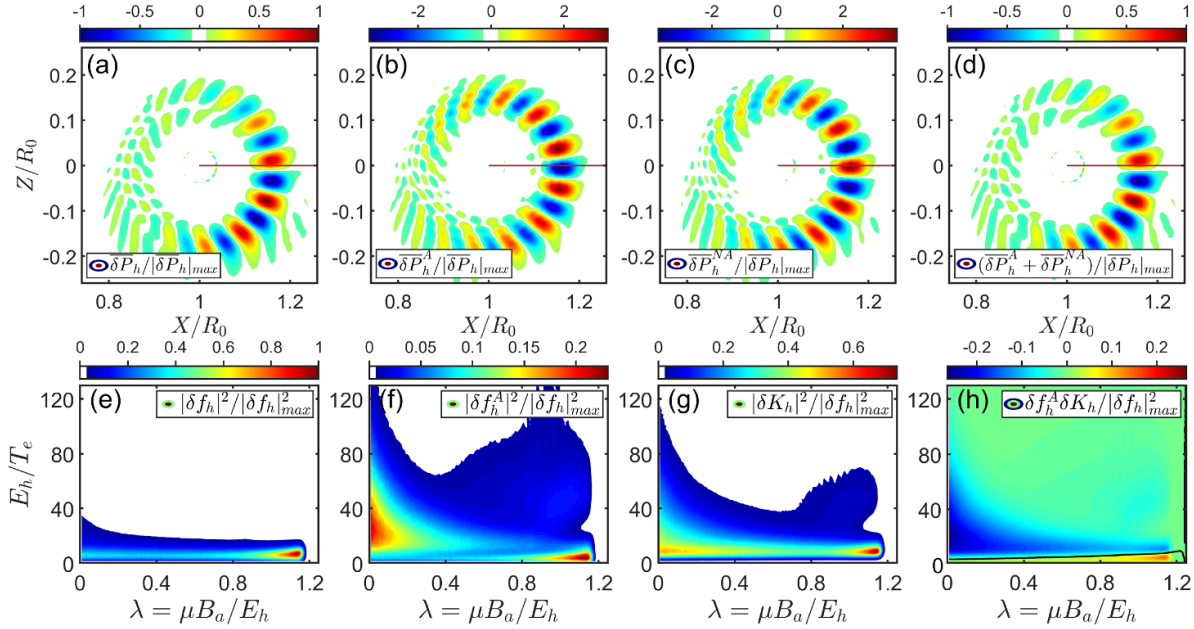

Figure 5. The 2D poloidal mode structure of EI pressure perturbations (upper row) and $|\delta f_h|^2$-intensities (bottom row) in case (I) at $T_h/T_e = 25$. Other details are the same as in figure 4.

that $\delta P_h = \delta P_h^A + \delta P_h^{NA}$ is satisfied. Comparing figures 5(*e*)–(*g*), the EI net response $|\delta f_h|^2$ only localizes in the narrow domain of $E_h/T_e \in [0, 10]$ and $\lambda > 1$, while both $|\delta f_h^A|^2$ and $|\delta K_h|^2$ distribute in a broader domain of E and λ, consistent with the corresponding pressure perturbation amplitudes with $|\delta P_h^A| \sim |\delta P_h^{NA}| \gg |\delta P_h|$. Specifically, $|\delta f_h^A|^2$ in figure 5(*f*) contains several parts including high-energy passing EIs ($E_h \sim T_h = 25T_e$ and $\lambda \sim 0$), high-energy trapped EIs ($E_h \sim T_h = 25T_e$ and $\lambda > 1$) and low-energy trapped EIs ($E_h \sim T_e \ll T_h$ and $\lambda > 1$); this is due to the FLR gyroaveraging effect $J_0(k_\perp \rho_h)$ in equation (20): for high-energy passing EIs and low-energy trapped EIs, the gyroaveraging effect $J_0(k_\perp \rho_h) \approx 1$ is negligible due to their small perpendicular velocity $v_\perp$, while the gyroaveraging effect of high-energy trapped EIs becomes important with $J_0(k_\perp \rho_h) \ll 1$ and thus significantly weakens their δf_h^A response. Meanwhile, $|\delta K_h|^2$ in figure 5(*g*) exhibits a similar structure to $|\delta f_h^A|^2$ in the high-energy regime, where the signs of fluid and kinetic responses are opposite

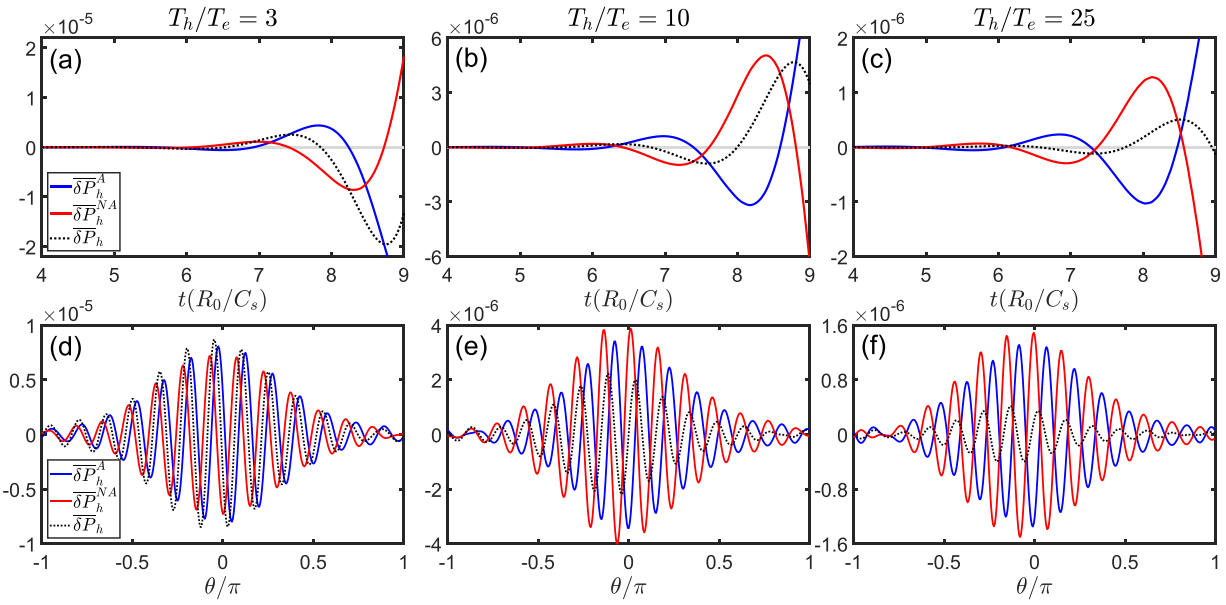

Figure 6. The time evolution (upper row) and poloidal variation (bottom row) of δP_h^A, δP_h^{NA} and δP_h. The results of $T_h/T_e = 3$, $T_h/T_e = 10$ and $T_h/T_e = 25$ simulations are shown from left to right columns.

with $\delta f_h^A \delta K_h < 0$, as shown in figure 5($h$), which supports the view that δf_h^A and δK_h mostly cancel each other in the high-energy regime due to large FOW screening, consistent with $k_\theta \rho_d \gg 1$ in table 1. In contrast, $\delta f_h^A \delta K_h > 0$ becomes positive in the bottom region of figure 5(h), corresponding to resonant EIs in the low-energy regime with $E_h \sim T_e$, the fluid and kinetic responses of which accumulate together and contribute to KBM destabilization. However, the fraction of the resonant EI population in the low-energy regime is much smaller than the total EI population with $f_{\rm res} \ll f_h$, as discussed in figures 3(c) and (f), and the majority of EIs in the high-energy regime exhibit near-zero net responses that induce thermal ion dilution for KBM stabilization, which dominates over the minor resonant EI destabilization. In a short, for the $T_h/T_e = 25$ simulation characterized by a large EI population at $E_h \sim T_h \gg T_e$, the EI fluid response $|\delta f_h^A|^2$ is dominated by high-energy passing EIs due to the stronger FLR gyroaveraging effect on high-energy trapped EIs, and FOW screening leads to cancellation between fluid and kinetic responses for most EIs, which results in $f_{\rm res} \ll f_h$ and thermal ion dilution that weakly stabilizes the KBM, despite the large $\beta_h \sim \beta_{e,i}$.

The time evolutions and poloidal structures of pressure perturbations δP_h, δP_h^A and δP_h^{NA} are compared for different T_h/T_e simulations in figure 6. It is clearly seen that the fluid component δP_h^A and kinetic component δP_h^{NA} accumulate together at $T_h/T_e = 3$ and cancel each other at $T_h/T_e = 25$. The accumulation occurs with a relatively weak FOW of $k_\theta \rho_d \lesssim 1$, which is valid for helium ash when $n_h \ll n_e$, $T_h/T_e \sim 1$ and $\beta_h \ll \beta_{e,i}$. The cancellation occurs with a strong FOW of $k_\theta \rho_d \gg 1$, which is valid for the interplay between NBI EIs and KBMs in small or medium size tokamaks. In addition, the fluid EI results from dropping the kinetic response-related term $\{F\}$ in equation (26) of EI model B are represented by the blue dashed line in figure 1, which exhibits a quantitative difference in ω_r and a qualitative difference in γ compared with the comprehensive model results. In order to accurately describe the EI–KBM interaction process, both EI fluid and kinetic responses should be kept over the full T_h/T_e range.

3.2. *Non-perturbative EI influence on the KBM in the long-wavelength regime of $k_\theta \rho_d \ll 1$*

Next, we carry out T_h/T_e scan simulations for case (II) using $m_h/m_p = 0.01$, which consequently decreases the EI FLR and EI FOW by a factor of 10 and increases the orbit frequencies of ω_ϕ, ω_θ and ω_b by a factor of 10; the precession frequency of $\omega_{\rm pre}$ remains the same as in case (I) as it depends on energy rather than mass. From table 1, the dimensionless orbit frequencies and widths of $T_h/T_e = 25$ in case (II) cover the parameter regimes of ($\beta_h \sim \beta_{e,i}$, $T_h/T_e \gg 1$, $k_\theta \rho_d \ll 1$) and can be analogous to alpha-particle interaction with Alfvénic modes in ITER, which are typically characterized by small dimensionless orbits and bounce-averaged dynamics [29].

The dependences of KBM ω_r and γ on T_h/T_e are compared between cases (I) and (II) in figures 7(a) and (b). It can be seen that both ω_r and γ increase monotonically with increasing T_h/T_e in case (II), variations of which become non-perturbative with $\Delta\omega_r/\omega_r \sim 50\%$ and $\Delta\gamma/\gamma \sim 130\%$ being much larger than in case (I) over the range of $T_h/T_e \in [1, 35]$. Specifically, in the regime of $T_h/T_e \sim 1$, EIs can weakly destabilize the KBM with $\beta_h \ll \beta_{e,i}$ in both case (I) and case (II), influences of which are perturbative and no longer discussed here. In the regime of $T_h/T_e \gg 1$, EIs can strongly destabilize the KBM with $\beta_h \sim \beta_{e,i}$ in case (II) rather than asymptotically approaching the dilution limit, which implies that most EIs can effectively interact with the KBM and suffer negligible FOW screening, consistent with $k_\theta \rho_d \ll 1$ in

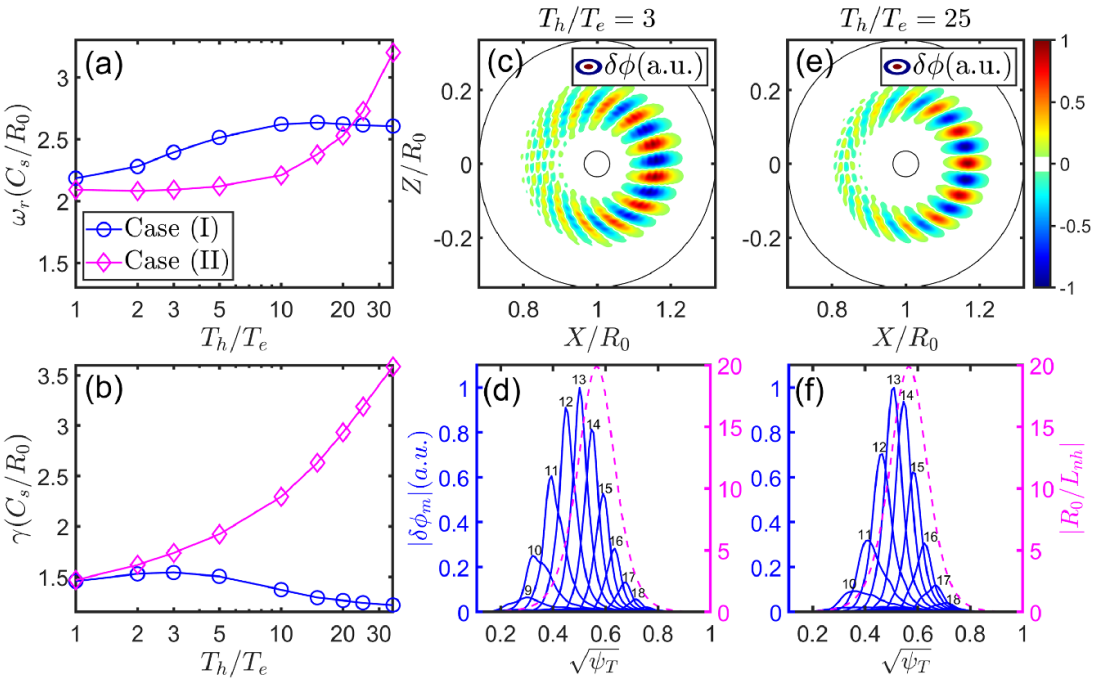

Figure 7. Comparisons of the $n = 10$ KBM dispersion relation between cases (I) and (II) in table 1. The dependences of KBM (*a*) real frequency ω_r and (*b*) growth rate γ on EI–thermal electron temperature ratio T_h/T_e. The blue-circle line represents the case (I) results in figure 1, and the magenta-diamond line represents the case (II) results using $m_h/m_i = 0.01$, which decreases EI FLR $k_\theta\rho_h$ and EI FOW $k_\theta\rho_d$ by a factor of 10 compared with case (I). The middle and right columns show the mode structure of electrostatic potential $\delta\phi$ in case (II) at $T_h/T_e = 3$ and $T_h/T_e = 25$, respectively.

table 1. The $\delta\phi$ mode structures of case (II) are shown in figure 7, where the $T_h/T_e = 3$ results are similar to the thermal ion limit in figures 2(*a*) and (d) with negligible EI modification; it is obvious that the $T_h/T_e = 25$ results are affected by the radial profile of the EI pressure gradient, which confirms the non-perturbative EI influence in addition to the large variations of ω_r and γ.

The EI pressure perturbation and $|\delta f|^2$-intensity from the $T_h/T_e = 25$ simulation of case (II) are shown in figure 8, where FLR and FOW are an order of magnitude smaller than in case (I). As shown in figures 8(*a*)–(*d*), the amplitudes of total δP_h become comparable to its fluid component δP_h^A and kinetic component δP_h^{NA}, implying a weak FOW screening effect, as expected, which satisfies $\delta P_h = \delta P_h^A + \delta P_h^{NA}$ with a finite poloidal phase shift. The EI $|\delta f_h|^2$-intensities in case (II) become drastically different from case (I); the EI net response $|\delta f_h|^2$ consists of both high-energy passing EI and low-energy trapped EI regions in figure 8(*e*), whereas $|\delta f_h|^2$ is only dominated by low-energy trapped EIs in figure 5(*e*). $|\delta f_h^A|^2$ in figure 8(*f*) peaks in the pitch angle range of $\lambda > 1$ and energy range of $E_h/T_e \in [1, 50]$, due to the smallness of the FLR gyroaveraging effect with $J_0(k_\perp\rho_h) \approx 1$ and large EI population at $E_h \sim T_h = 25T_e$, the mechanism of which is similar to figure 4(*f*) and discussed in detail in section 3.1. $|\delta K_h|^2$ in figure 8(*g*) not only distributes in the trapped region but also governs $|\delta f_h|^2$ in the passing region of $E_h/T_e \in [25, 75]$ and $\lambda < 1$, which implies that the high-energy passing EIs with small FOW in case (II) can resonantly interact with the KBM. It should be pointed out that for passing particles with a small dimensionless orbit of $k_\theta\rho_d \ll 1$ and large orbit frequency of $\omega_\phi \sim \omega_\theta \gg \omega$, the resonance condition of $\omega = n\omega_\phi - p\omega_\theta$ can be satisfied locally around the rational surface of $q = p/n$, which can be intuitive by taking $\omega_\phi = v_{||}/R_0$ and $\omega_\theta = v_{||}/qR_0$ in the well-circulating limit and approximating $n\omega_\phi \approx p\omega_\theta$, consistent with the runaway electron resonance with MHD modes [34] and energetic electron excitation of the ellipticity-induced Alfvén eigenmode in a recent EAST experiment [35]. The characteristics of trapped and passing EI resonances can also be reflected through the corresponding pressure perturbations in figure 9. It is seen that the passing EI-integrated δP_h^p peaks at each rational surface with a radially discretized structure in figure 9(*a*), while the trapped EI-integrated δP_h^t in figure 9(*b*) is much smoother in a radial direction without localization, and the amplitude of δP_h^p is larger than δP_h^t by a factor of 2, which indicates that the high-energy passing EIs dominate over low-energy trapped EIs for non-perturbative destabilization of the KBM at $T_h/T_e = 25$ for case (II) in figure 7(*b*). On the other hand, it should be noted that for the high-energy trapped EI region marked by the black dashed boxes in figures 8(*e*)–(*h*), the EI fluid and kinetic responses are opposite in sign, indicated by the negative $\delta f_h^A \delta K_h < 0$, and mostly cancel each other, resulting in a near zero net response for high-energy trapped EIs. However, unlike strong FOW screening in case (I), the mechanism of this cancellation in case (II) in the regime of $k_\theta\rho_d \ll 1$ is due to the lack of resonance conditiona with $\omega \ll \omega_d$ for high-energy trapped EIs, which agrees with the finding in earlier studies [10, 13, 14] that the zero-orbit-width trapped EI fluid potential energy δW_f and kinetic potential energy δW_k can destabilize and stabilize KBM, respectively (i.e. opposite effects). In the appendix we

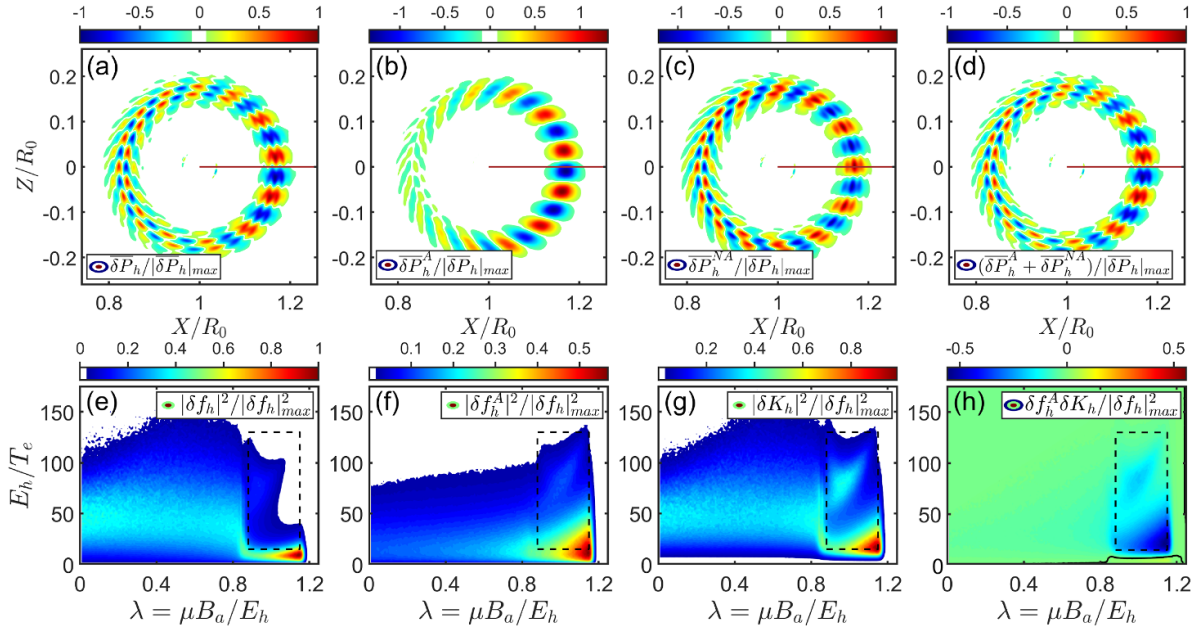

Figure 8. The 2D poloidal mode structure of EI pressure perturbations (upper row) and $|\delta f_h|^2$-intensities (bottom row) in case (II) at $T_h/T_e = 25$. The other details are the same as in figure 4.

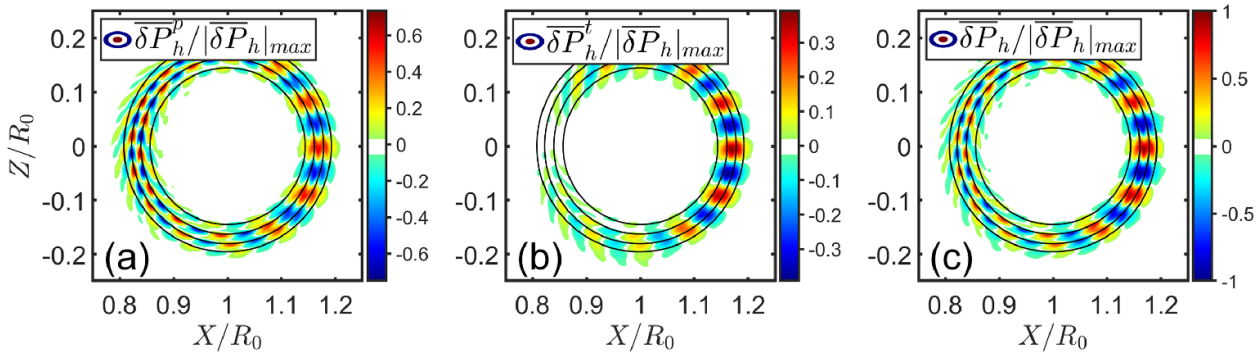

Figure 9. The 2D poloidal mode structures of EI pressure perturbations in case (II) at $T_h/T_e = 25$ for (a) passing particle contribution δP_h^p, (b) trapped particle contribution δP_h^t and (c) total $\delta P_h = \delta P_h^p + \delta P_h^t$, which are normalized by the maximal amplitude of δP_h, i.e. $\max(|\delta P_h|)$. The black lines represent the rational surfaces of $q = 1.2, 1.3, 1.4, 1.5$ from inner to outer regions.

analytically derive the trapped EI fluid and kinetic responses to KBM electromagnetic fluctuations based on EI model B, and prove the cancellation between MHD ballooning-interchange and KPC (i.e. terms $\{E\}$ and $\{F\}$ in equation (26)) consistent with GTC simulation results.

3.3. Nonlinear EI transport by KBMs

We further extend the linear analysis of KBM stability to the nonlinear regime to study the influences of EIs on KBM nonlinear saturation and plasma anomalous transport. As well as $n = 10$ KBM electromagnetic fluctuations, the zonal flow $\delta\phi_{00}$ and zonal current $\delta A_{||00}$ are also kept in the nonlinear simulations which can be generated through a beat-driven process with a twice linear growth rate $\gamma_Z = 2\gamma_{\rm KBM}$; this can effectively regulate the $n = 10$ KBM and lead to nonlinear saturation [19]. It should be noted that all simulations in this work were carried out with collisionless plasmas, and the primary dissipation mechanisms in nonlinear simulations include nonlinear Landau damping by thermal ions and EI FOW screening. The time evolutions of volume-averaged KBM $\delta\phi$ perturbation, thermal ion particle diffusivity D_i, heat conductivity χ_i and EI particle diffusivity D_h are compared between cases (I) and (II) at $T_h/T_e = 3$ and $T_h/T_e = 25$, as shown in figure 10, corresponding to the EI dimensionless parameters listed in table 1.

From figures 10(a)–(c), the slopes of $\delta\phi$, D_i and χ_i history curves in the linear stage are consistent with KBM growth rates in figures 1(b) and 7(b), and become steeper/flatter for destabilization/stabilization compared with the thermal ion limit results indicated by black solid lines. The KBMs reach initial saturation at the turning points of each curve, where the saturation and transport levels are measured. It can be seen that KBM saturation is insensitive to the linear growth rate due to the zonal flow regulation mechanism, which leads to

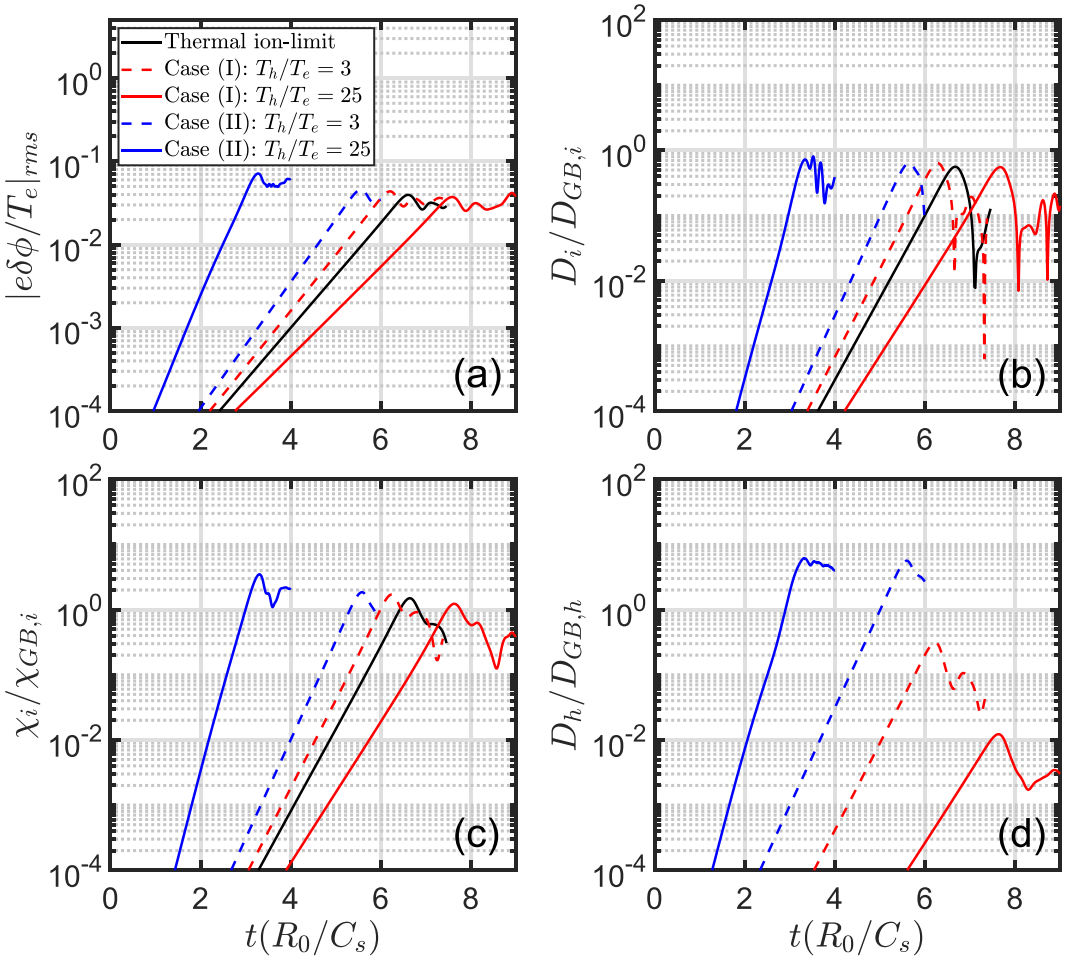

Figure 10. Nonlinear GTC results for (*a*) $n = 10$ KBM electrostatic potential amplitude $|e\delta\phi/T_e|_{\rm rms}$ (where $|\cdots|_{\rm rms}$ denotes the root-mean-squared operation), (*b*) thermal ion particle diffusivity $D_i/D_{GB,i}$, (*c*) thermal ion heat conductivity $\chi_i/\chi_{GB,i}$ and (*d*) EI particle diffusivity $D_h/D_{GB,h}$. Gyrobohm units are used for transport coefficient normalizations with $D_{GB,\alpha} = \chi_{GB,\alpha} = \rho_\alpha^* cT_e/eB_a$, where $\alpha = i,h$ and $\rho_\alpha^* = \rho_\alpha/a$ is the gyroradius normalized by the tokamak minor radius.

the close saturation levels of $\delta\phi$, D_i and χ_i at $T_h/T_e = 3$ and $T_h/T_e = 25$ for case (I) and case (II), although the results for $T_h/T_e = 25$ in case (II) are relatively higher than the others but still have the same order of magnitude; thus the influences of EIs on the KBM nonlinear saturation level and thermal ion transport coefficients can be ignored. However, the EI particle diffusivity D_h in figure 10(*d*) significantly varies between different simulations; this is mostly determined by the resonant EI population $f_{\rm res}$ and resonant energy E_h. It can be seen from figure 10(*d*) that the D_h saturation level in the $T_h/T_e = 25$ simulation of case (II) (blue solid line) is more than one order of magnitude larger than in the $T_h/T_e = 3$ simulation of case (I) (red dashed line), and is more than two orders of magnitude larger than in the $T_h/T_e = 25$ simulation of case (I) (red solid line), consistent with the distribution domain sizes of $|\delta f_h|^2$ and f_h as shown in figures 3 and 8(*e*). In addition, the D_h saturation level in the $T_h/T_e = 3$ simulation of case (II) (blue dashed line) is also more than an order of magnitude larger than in the $T_h/T_e = 3$ simulation of case (I) (red dashed line) in figure 10(*d*), which are both dominated by precessional drift resonance of $\omega = n\omega_{\rm pre}$ at the same E_h, while the FLR and FOW in case (II) are smaller than in case (I) by a factor of 10, which minimizes the FLR gyroaveraging and FOW screening effects and thus enhances EI transport.

Figure 11 illustrates the dependence of the saturation levels for the electrostatic potential and the transport coefficients of thermal ions and EIs on the ratio T_h/T_e, with all levels measured at the time of saturation. The scaling trends are consistent with the physical picture presented in figure 10. Notably, the saturation level of D_h in case (I) exhibits a dependence on T_h that is consistent with EI transport driven by the ITG [36, 37]. This agreement underscores the significance of FOW and FLR effects. It further demonstrates that EI transport remains significant when $T_h \gtrsim T_e$ and becomes negligible for $T_h/T_e > 10$. In contrast, for case (II), D_h increases markedly with T_h in the regime where $T_h \gg T_e$. This suggests that resonance between EIs and KBM in the long-wavelength regime, occurring via transit motion resonance, can substantially alter the physical nature of transport.

In summary, for high-temperature EIs with $T_h/T_e = 25$, KBMs can cause significant EI transport in the long-wavelength regime of $k_\theta\rho_d \ll 1$ due to passing EI transit motion resonance, resulting in a much larger EI particle diffusivity compared with thermal ions with $D_h \gg D_i$. In

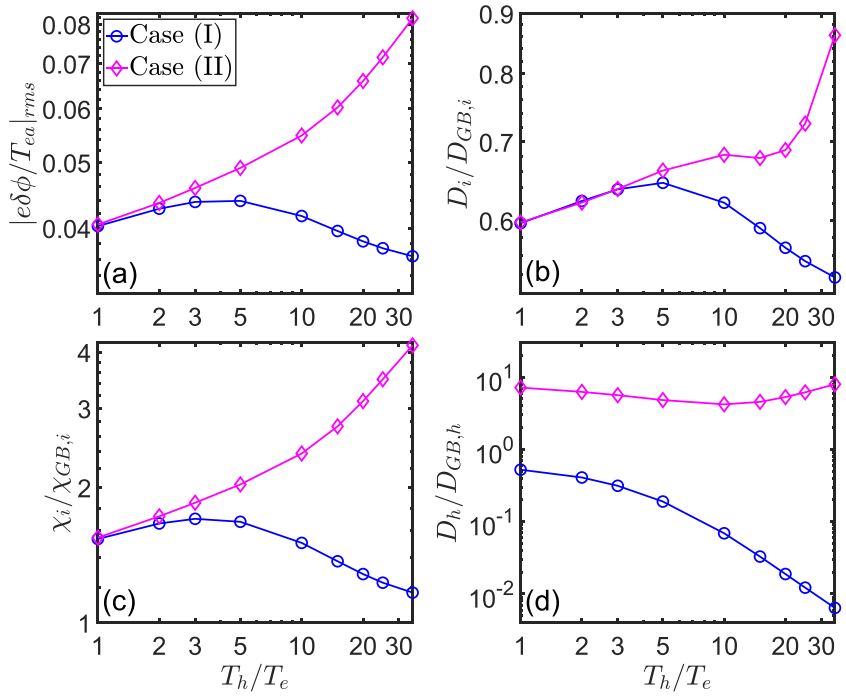

Figure 11. Comparisons of nonlinear simulation results for a $n = 10$ KBM between cases (I) and (II) in table 1 at the time of saturation. The dependences of KBM (*a*) electrostatic potential amplitude $|e\delta\phi/T_e|_{\rm rms}$, (*b*) thermal ion particle diffusivity $D_i/D_{GB,i}$, (*c*) thermal ion heat conductivity $\chi_i/\chi_{GB,i}$ and (*d*) EI particle diffusivity $D_h/D_{GB,h}$ on the EI–thermal electron temperature ratio T_h/T_e. Other details are the same as in figure 10.

contrast, EI transport can be greatly reduced in the short-wavelength regime of $k_\theta\rho_d \gg 1$ due to strong FOW screening; particle diffusivity is much smaller than thermal ion diffusivity with $D_h \ll D_i$. For low-temperature EIs with $T_h/T_e = 3$ and $m_h/m_p = 1$, EI transport is similar to that of thermal ions when $D_h \sim D_i$. It should be noted that recent AUG experiments have observed the strong impacts of EIs on edge-localized modes (ELMs), which significantly modify the mode amplitude and frequency spectrum as well as the nonlinear crash, where the wave–particle resonances between EIs and $n \sim$ 8–10 ELMs play a leading role [38]. Although we focus here on the EI transport induced by core KBMs, the interaction mechanisms proposed in this work are general and can be applied to edge KBMs characterized by a high-n spectrum around $k_\theta\rho_i \sim 1$ (ρ_i denotes the thermal ion FLR), which cause negligible EI transport due to a large FOW screening effect.

4. Summary

In this work, the influences of EIs on KBM stability were investigated based on global gyrokinetic simulations over a wide range of EI orbit frequencies and orbit sizes. In order to delineate the separate effects of EI fluid and kinetic responses, a new gyrokinetic EI model was formulated and implemented in GTC code based on the Chen–Hasegawa theory [20], which splits the perturbed distribution into adiabatic fluid convection response and non-adiabatic kinetic response as $\delta f_h = \delta f_h^A + \delta K_h$ and solves each dynamic, showing excellent agreements with the conventional δf-method. By performing KBM simulations with EIs using both the conventional δf-method and the newly developed split scheme, the EI $|\delta f|^2$-intensity in (E, λ) phase space and perturbed pressure in real space can be evaluated for the EI net response together with its fluid and kinetic parts, which are consistent with each other satisfying $\delta P_h = \delta P_h^A + \delta P_h^{NA}$. The EI–KBM resonance condition, EI FLR/FOW and EI drive strength rely on the key dimensionless parameters of T_h/T_e, $k_\theta\rho_d$ and β_h, which mostly determine the physical process of EI–KBM interaction. The results of three typical parameter regimes are summarized as follows:

(i) For low-temperature minor ion species with ($\beta_h \ll \beta_{e,i}$, $T_h/T_e \sim 1$, $k_\theta\rho_d \sim 1$), such as helium ash, EIs can resonantly interact with the KBM through transit motion resonance and precessional drift resonance with $\omega \sim \omega_{\rm tr} \sim n\omega_{\rm pre}$, and give comparable fluid and kinetic responses with modest FOW screening that destabilize the KBM; influences on KBM linear stability and nonlinear saturation level are perturbative due to the small drive strength of $\beta_h \ll \beta_{e,i}$. The KBM-induced EI particle diffusivity is of the same order as thermal ions as $D_h \sim D_i$.

(ii) For NBI EI and short-wavelength KBMs with ($\beta_h \sim \beta_{e,i}$, $T_h/T_e \gg 1$, $k_\theta\rho_d \gg 1$), the EIs stabilize the KBM through thermal ion dilution with perturbative influences, attributed to the fact that strong FOW screening leads to cancellation between fluid and kinetic responses in the high-energy regime $E_h \sim T_h \gg T_e$, resulting in a near zero net response for the majority of the EI population, while the fraction of resonant EIs in the low-energy regime of $E_h \sim T_e$ is much smaller than the total EI population with $f_{\rm res} \ll f_h$; the small drive cannot overcome

stabilization of thermal ion dilution despite the large $\beta_h \sim \beta_{e,i}$. Since the KBM electromagnetic fluctuations are greatly reduced due to large FOW screening, EI particle diffusivity becomes much smaller than that of thermal ions with $D_h \ll D_i$.

(iii) For alpha particles and long-wavelength KBMs with ($\beta_h \sim \beta_{e,i}$, $T_h/T_e \gg 1$, $k_\theta \rho_d \ll 1$), the high-energy passing EIs can non-perturbatively destabilize the KBM through transit motion resonance around the rational surface $q = p/n$ (p is an integer), where the large toroidal frequency $\omega_\phi \gg \omega$ and poloidal frequency $\omega_\theta \gg \omega$ mostly cancel each other and satisfy $\omega = n\omega_\phi - p\omega_\theta$, and the EI particle diffusivity is much larger than thermal ion diffusivity, with $D_h \gg D_i$. The high-energy trapped EI net response is near zero due to mismatch of the resonance condition with $\omega \ll n\omega_{\rm pre}$, which is confirmed by both simulation and theory. The KBM mode structure adapts to the EI drive radial profile of $|R_0/L_{n,h}|$ to a certain degree due to the non-perturbative influence of passing EIs.

The KBM nonlinear saturation level is barely affected by EIs in all regimes due to the dominant zonal flow regulation mechanism [19]. It is worth mentioning that points (i) and (ii) represent the traditional picture, being consistent with EI–ITG interaction in [36, 37], highlighting the importance of FOW and FLR and showing that the EI transport coefficient maximizes at $E_h = 2T_e$ and becomes negligible at $E_h/T_e > 10$. Item (iii) introduces the new mechanism of transit motion resonance between small dimensionless orbit EIs and low-frequency drift Alfvénic waves, which dominates EI–KBM interaction in the long-wavelength limit, either for low-n modes or for large machine sizes. It should also be pointed out that a global toroidal geometry with concentric circular poloidal section was used in this study to demonstrate the direct effects of EIs on the KBM, the central peaked EI pressure might also increase the Grad–Shafranov shift and alter the boundaries of the KBM's first and second stability region as an indirect effect; this will be considered in future work.

Acknowledgments

J Bao and W J Sun acknowledge useful discussions with Professors Liu Chen, W W Heidbrink and Ruirui Ma. This work is supported by National Natural Science Foundation of China under Grant Nos. 12025508, 12275351 and 11905290; the National Key R&D Program of China under Grant No. 2024YFE03170004; the Strategic Priority Research Program of Chinese Academy of Sciences under Grant Nos. XDB0500302 and XDB0790202; and the start-up funding of Institute of Physics, Chinese Academy of Sciences under Grant No. Y9K5011R21.

Appendix. trapped EI response function in the zero-orbit-width limit

To interpret the opposite phase and cancellation between MHD ballooning-interchange and KPC for high-energy trapped EIs with mass ratio $m_h/m_i = 0.01$ in the regime of $T_h \gg T_{e,i}$ from GTC simulation, in this appendix we theoretically derive terms $\{B\}$ and $\{C\}$ for EI species in the Chen–Hasegawa gyrokinetic vorticity equation described by equation (19), which corresponds to MHD ballooning-interchange and KPC from the integration of δf_h^A and δK_h in velocity space. In order to delineate the role of the EI pressure gradient in a concise manner, EI FLR and FOW are not taken into account due to the small EI mass ratio. The EI diamagnetic drift frequencies are set to be consistent with GTC simulation, namely $\omega_{*T,h} = 0$ due to the uniform EI temperature profile and $\omega_{*n,h} \gg \omega$ due to $\omega \sim \omega_{*p,i}$ and $T_h \gg T_{e,i}$, which indicates that EI pressure (density) gradient-related terms dominate over the adiabatic and non-adiabatic responses. Moreover, the isotropic Maxwellian and electromagnetic Alfvénic polarizations of $\delta\phi = \delta\psi$ are applied. Then the EI adiabatic response in equation (21) reduces to

$$\delta {f^A}_h = -\frac{Z_h}{T_{h0}}\delta\psi\,\frac{\omega_{*n,h}}{\omega} f_{h0}. \tag{34}$$

Considering equations (28) and (29), the MHD ballooning-interchange in equation (19) becomes

$$\begin{aligned}\text{term}\{B\} &= -\frac{4\pi i\omega}{c}\frac{\mathbf{b_0}\times\boldsymbol{\kappa}}{B_0}\cdot\nabla\left(\delta P^A_{||h} + \delta P^A_{\perp h}\right)\\ &= -\frac{8\pi}{c^2}\frac{Z_h^2 n_{h0}}{T_{h0}}\omega_{*n,h}\omega_{D,h}\delta\psi,\end{aligned} \tag{35}$$

where $\omega_{D,h} = -i\,\frac{cT_{h0}}{Z_h B_0}\mathbf{b_0}\times\boldsymbol{\kappa}\cdot\nabla$. It should be noted that equation (35) takes into account the adiabatic responses of both passing and trapped EIs, namely the MHD ballooning-interchange arises from the fluid convection response of particles of all orbit types. For comparison, the KPC is sensitive to pitch angle and different between passing and trapped EIs, which relies on the particular motion frequency and wave–particle resonance condition. It is seen from figure 8 that in GTC simulation the cancellation mainly occurs in regime of high-energy trapped EIs. Following the approach in reference [39], we solve the non-adiabatic response for trapped EIs by using the deeply trapped approximation and performing the bounce-average operation $\overline{(\ldots)} = \oint(\ldots)(\mathrm{d}l/v_{||})\tau_b$ on equation (18), where $\tau_b = \oint(\mathrm{d}l/v_{||})$ is the bounce period. Then we obtain

$$\delta K_h^{\rm trap} = -\frac{\overline{\omega_{d,h}\delta\psi}}{\omega - \overline{\omega}_{d,h}}\frac{Z_h}{T_{h0}}\frac{\omega_{*n,h}}{\omega} f_{h0}, \tag{36}$$

where $\overline{\omega}_{d,h}$ denotes the precession frequency, which can be approximated as $\overline{\omega}_{d,h} \approx \omega_{D0,h} = -i\,\frac{cT_{h0}}{Z_h B_0}\mathbf{b_0}\times\boldsymbol{\kappa}\cdot\nabla|_{\theta=0}$ based on the deeply trapped approximation, and $\overline{\omega_{d,h}\delta\psi} \approx \overline{\omega}_{d,h}\delta\psi$ can be applied for ballooning mode structures with $|nq - m| \ll 1$ [39]. By integrating equation (36) in velocity space for all trapped EIs, term $\{C\}$ in equation (19) can be expressed as

$$\begin{aligned}\text{term}\{C\} &= -\frac{4\pi i\omega}{c^2} Z_h \langle \mathbf{v_d}\cdot\nabla\delta K_h^{\rm trap}\rangle_{v,h}\\ &= \frac{8\pi}{c^2} f_t \frac{Z_h^2 n_{h0}}{T_{h0}} R_5\left(\sqrt{\zeta}\right)\omega_{*n,h}\omega_{D0,h}\delta\psi,\end{aligned} \tag{37}$$

where $f_t = \frac{1}{n_{h0}} \int_{\rm trap} f_{h0} \mathbf{dv} = \sqrt{1 - \lambda_{\rm min} \frac{B_0}{B_a}}$ denotes the trapped EI fraction on the poloidal plane, $\lambda_{\rm min} = B_a / B_{\rm max}$ represents the lower limit of trapped particle pitch angle, B_a is the on-axis magnetic field strength and B_0 and $B_{\rm max}$ are the local and maximal magnetic field strengths on the flux surface, respectively. $R_5(\sqrt{\zeta})$ is the deeply trapped particle response function with $\zeta = \omega / \omega_{D0,h}$

$$R_5\left(\sqrt{\zeta}\right) = \frac{3}{4} + \frac{1}{2}\zeta + \zeta^2 + (\zeta)^{5/2} Z\left(\sqrt{\zeta}\right), \tag{38}$$

where $Z(x) = \frac{1}{\sqrt{\pi}} \int_{-\infty}^{+\infty} \frac{\exp(-t^2)}{t-x} {\rm d}t$ is the plasma dispersion function.

For $T_h \gg T_{e,i}$, the precessional drift resonance condition is no longer satisfied when $\zeta = \omega / \omega_{D0,h} \ll 1$. Combining equations (35) and (37), the ratio between MHD ballooninginterchange and KPC in the limit of $\zeta \to 0$ can be readily obtained as

$$\left.\frac{\text{term}\{C\}}{\text{term}\{B\}}\right|_{\zeta \to 0} \sim -f_t R_5(0) \sim -\frac{3}{4} f_t. \tag{39}$$

Note that the $3/4$ factor in equation (39) is due to the deeply trapped approximation, the ratio is close to $-f_t$ and indicates that the KPC of trapped EIs will cancel their fraction in MHD ballooning-interchange, leading to the zero trapped EI response to KBM electromagnetic fluctuations when $\omega \ll \omega_{D0,h} \sim \overline{\omega}_{d,h}$. This physical picture is similar to the trapped electron effect in ITG mode, since the precessional drift direction is opposite to the ITG propagation direction for most trapped electrons and no resonant interaction happens, which also lead to the zero trapped electron response to ITG fluctuation rather than an adiabatic one [40]. Interestingly, the consequences of the zero trapped electron response for ITG and the zero trapped EI response for the KBM are opposite—the former destabilizes ITG by decreasing the adiabatic electron shielding effect in the dielectric constant (note that plasma adiabatic response to $\delta\phi$ induces a shielding/screening effect on electrostatic modes rather than MHD ballooning-interchange drive induced through $\delta\psi$). These theoretical analyses can explain the opposite contribution between MHD ballooning-interchange and KPC for high-energy trapped EIs, as shown in figure 8.

ORCID iDs

W.J. Sun 0009-0007-8132-913X
J. Bao 0000-0002-2890-0700
C. Dong 0000-0001-8229-2198
W.L. Zhang 0000-0002-7136-2119
G. Dong 0000-0002-7734-3736
Z. Lin 0000-0003-2007-8983
J.T. Cao 0009-0004-8058-310X
Z.Y. Qiu 0000-0002-7548-8819
H.S. Cai 0000-0002-2500-3721
D. Li 0000-0002-4643-597X

References

[1] Tang W.M. *et al* 1980 Kinetic-ballooning-mode theory in general geometry *Nucl. Fusion* **20** 1439
[2] Cheng C.Z. 1982 High-*n* collisionless ballooning modes in axisymmetric toroidal plasmas *Nucl. Fusion* **22** 773
[3] Chen L. and Zonca F. 2016 Physics of Alfvén waves and energetic particles in burning plasmas *Rev. Mod. Phys.* **88** 015008
[4] Jian X. *et al* 2023 Experimental validation of a kinetic ballooning mode in high-performance high-bootstrap current fraction fusion plasmas *Phys. Rev. Lett.* **131** 145101
[5] Snyder P.B. *et al* 2009 Development and validation of a predictive model for the pedestal height *Phys. Plasmas* **16** 056118
[6] Gary M.S. 2018 Theory of transport in high bootstrap fraction H-modes with internal transport barriers *Nucl. Fusion* **58** 115001
[7] Citrin J. and Mantica P. 2023 Overview of tokamak turbulence stabilization by fast ions *Plasma Phys. Control. Fusion* **65** 033001
[8] Cooper W.A. 1982 Alpha-particle diamagnetic drift effects on tokamak ballooning stability *Nucl. Fusion* **22** 835
[9] Tsang K.T. and Sigmar D.J. 1981 Stabilization of ballooning modes by energetic particles in tokamaks *Nucl. Fusion* **21** 1227
[10] Rosenbluth M.N. *et al* 1983 Energetic particle stabilization of ballooning modes in tokamaks *Phys. Rev. Lett.* **51** 1967
[11] Biglari H. and Chen L. 1991 Unified theory of resonant excitation of kinetic ballooning modes by energetic ions and alpha particles in tokamaks *Phys. Rev. Lett.* **67** 3681
[12] Tsai S.-T. and Chen L. 1993 Theory of kinetic ballooning modes excited by energetic particles in tokamaks *Phys. Fluids B* **5** 3284
[13] Spong D.A. *et al* 1985 Effects of trapped alpha particles on ballooning modes in tokamaks *Phys. Fluids* **28** 2494
[14] Spong D.A. *et al* 1987 Effects of alpha populations on tokamak ballooning stability *Phys. Scr.* **1987** 18
[15] Han H. *et al* 2022 A sustained high-temperature fusion plasma regime facilitated by fast ions *Nature* **609** 269–75
[16] Yong-Su N. *et al* 2025 How fast ions mitigate turbulence and enhance confinement in tokamak fusion plasmas *Nat. Rev. Phys.* **7** 190–202
[17] Lin Z. *et al* 1998 Turbulent transport reduction by zonal flows: massively parallel simulations *Science* **281** 1835–7
[18] Dong G. *et al* 2017 Gyrokinetic particle simulations of the effects of compressional magnetic perturbations on drift-Alfvénic instabilities in tokamaks *Phys. Plasmas* **24** 081205
[19] Dong G. *et al* 2019 Nonlinear saturation of kinetic ballooning modes by zonal fields in toroidal plasmas *Phys. Plasmas* **26** 010701
[20] Chen L. and Hasegawa A. 1991 Kinetic theory of geomagnetic pulsations: I. Internal excitations by energetic particles *J. Geophys. Res.* **96** 1503
[21] Tang W.M. 1978 Microinstability theory in tokamaks *Nucl. Fusion* **18** 1089
[22] Cheng C.Z. 1982 Kinetic theory of collisionless ballooning modes *Phys. Fluids* **25** 1020
[23] Kennedy D. *et al* 2023 Electromagnetic gyrokinetic instabilities in STEP *Nucl. Fusion* **63** 126061
[24] Kennedy D. *et al* 2024 On the importance of parallel magnetic-field fluctuations for electromagnetic instabilities in STEP *Nucl. Fusion* **64** 086049
[25] Holod I. *et al* 2009 Electromagnetic formulation of global gyrokinetic particle simulation in toroidal geometry *Phys. Plasmas* **16** 122307

[26] Deng W. *et al* 2012 Gyrokinetic simulation model for kinetic magnetohydrodynamic processes in magnetized plasmas *Nucl. Fusion* **52** 023005
[27] Bao J. *et al* 2017 A conservative scheme of drift kinetic electrons for gyrokinetic simulation of kinetic-MHD processes in toroidal plasmas *Phys. Plasmas* **24** 102516
[28] Zonca F. *et al* 1996 Kinetic theory of low-frequency Alfvén modes in tokamaks *Plasma Phys. Control. Fusion* **38** 2011–28
[29] Zonca F. *et al* 2007 Electron fishbones: theory and experimental evidence *Nucl. Fusion* **47** 1588
[30] Lu Z. *et al* 2018 Kinetic effects of thermal ions and energetic particles on discrete kinetic BAE mode generation and symmetry breaking *Nucl. Fusion* **58** 082021
[31] Ma R. *et al* 2015 Global theory of beta-induced Alfvén eigenmode excited by energetic ions *Phys. Plasmas* **22** 092501
[32] Meng G. *et al* 2020 Effects of the non-perturbative mode structure on energetic particle transport *Nucl. Fusion* **60** 056017
[33] Wang Z. *et al* 2013 Radial localization of toroidicity-induced Alfven eigenmodes *Phys. Rev. Lett.* **111** 145003
[34] Breizman B.N. *et al* 2019 Physics of runaway electrons in tokamaks *Nucl. Fusion* **59** 083001
[35] Su P. *et al* 2024 Bursting core-localized ellipticity-induced Alfvén eigenmodes driven by energetic electrons during EAST ohmic discharges *Nucl. Fusion* **64** 036019
[36] Zhang W.L. *et al* 2008 Transport of energetic particles by microturbulence in magnetized plasmas *Phys. Rev. Lett.* **101** 095001
[37] Zhang W.L. *et al* 2010 Scalings of energetic particle transport by ion temperature gradient microturbulence *Phys. Plasmas* **17** 055902
[38] Dominguez-Palacios J. *et al* 2025 Effect of energetic ions on edge-localized modes in tokamak plasmas *Nat. Phys.* **21** 43–51
[39] Bao J. *et al* 2023 Global simulations of kinetic-magnetohydrodynamic processes with energetic electrons in tokamak plasmas *Nucl. Fusion* **64** 016004
[40] Lin Z. *et al* 2007 Global gyrokinetic particle simulations with kinetic electrons *Plasma Phys. Control. Fusion* **49** B163–72